The Biotite to Phengite Reaction and Mica-dominated Melting in Fluid + Carbonate-saturated Pelites at High Pressures

TONNY B. THOMSEN* AND MAX W. SCHMIDT

INSTITUTE FOR MINERALOGY AND PETROLOGY, ETH ZÜRICH, CLASIUSSTRASSE 25, CH-8092 ZÜRICH, SWITZERLAND

RECEIVED NOVEMBER 27, 2006; ACCEPTED SEPTEMBER 19, 2008
ADVANCE ACCESS PUBLICATION OCTOBER 29, 2008

Subsolidus and melting experiments were performed at 2·0–3·7 GPa and 750–1300°C on a carbonated pelite in the model system K_2O–CaO–MgO–Al_2O_3–SiO_2–H_2O–CO_2 to define stabilities of potassic micas and fluid-present melting reactions. The biotite to phengite reaction occurs at pressures between 2·4 and 2·6 GPa for temperatures of 750–850°C, and the amphibole to clinopyroxene reaction from 2·0 GPa, 875°C to 2·5 GPa, 740°C. Dolomite is the carbonate phase stable at subsolidus conditions. The biotite to phengite reaction preserves K_2O, but is not H_2O conservative, as a fluid is produced from the decomposition of zoisite. Phengite + quartz control fluid-saturated melting at a pressure (P) >2·6 GPa, whereas biotite + quartz dominate at P <2·4 GPa. Incongruent melting occurs through the reactions phengite or biotite + zoisite + quartz/coesite + fluid = silicate melt + clinopyroxene + kyanite. Overstepping of the solidus, located at 850–950°C, results in 7–24 wt % metaluminous K-rich granitic melts. The experiments define the melting surface of the model system, projected from kyanite + quartz/coesite + fluid onto the K_2O–CaO–MgO plane. The solidus melts in the studied system occur at a peritectic point consuming mica + zoisite and forming clinopyroxene. With increasing temperature (T), carbonated pelites then evolve along a peritectic curve along which further clinopyroxene is produced until zoisite is exhausted. This is then followed by a peritectic curve consuming clinopyroxene and producing garnet. A comparison of CO_2-bearing with CO_2-free experiments from the literature suggests that the main effect of adding calcite to a continental sediment is not the minor shift of typically 20–30°C of reactions involving fluid, but the change in bulk Ca/(Mg + Fe) ratio stabilizing calcic phases at the expense of ferromagnesian phases. The experiments suggest that in most subduction zones, CO_2, H_2O and K_2O will be carried to depths in excess of 120–150 km through carbonates and K-micas, as partial melting occurs only at temperatures at the uppermost end of thermal models of subduction zones. Nevertheless, the release of fluid through P-induced decomposition of amphibole and zoisite provides some H_2O for arc magma formation. Melting at higher temperatures (e.g. resulting from slower burial rates or from incorporation of subducted crust into the mantle) will produce potassic granitic melts and provide a substantial volatile and K source for the formation of arc magmas.

KEY WORDS: *biotite to phengite reaction; carbonated pelite; high-pressure experiments; KCMASH–CO_2; subsolidus and melting reactions; H_2O, K_2O and CO_2 in subduction zones*

INTRODUCTION

Subsolidus reactions and melting in the crust are controlled either by the availability of fluids mainly composed of H_2O and CO_2 or, in the absence of a free fluid phase, by the stability of hydroxyl- and carbonate-bearing minerals. The latter control the recycling of volatile components into the mantle (Thompson, 1988; Ono, 1998; Schmidt & Poli, 1998; Vielzeuf & Schmidt, 2001). Natural marls are oceanic shelf or platform sediments (Bucher & Frey, 2002) composed of a carbonate and a pelitic component with possible volcanic ash and siliceous components in addition (Plank & Langmuir, 1998). Such marls or calc-silicates are present

*Corresponding author. Present address: Institute of Geological Sciences, University of Bern, CH-3012 Bern, Switzerland. Telephone: +41 (0)31 631 87 61. E-mail: thomsen@geo.unibe.ch

in minor volumes in most metamorphic high-*P* terranes and are widely distributed in the European Alps (Droop *et al.*, 1990; Enami *et al.*, 2004). Once subducted, such rocks have the potential to carry water, C, and K deep into the upper mantle, and may influence arc magmatism through devolatilization or silicate melting.

The dominant potassic mica in low-*P*, high-grade marls and pelites is biotite (e.g. Thompson, 1975; Ferry, 1976, 1983a, 1983b; Frey, 1978; Frank, 1983; Spear, 1995; Bucher & Frey, 2002), whereas in high-*P* marls, pelites and greywackes phengite is stable (e.g. Dachs, 1986; Spear, 1995; Domanik & Holloway, 2000; Ogasawara *et al.*, 2000; Bucher & Frey, 2002; Schmidt *et al.*, 2004). Phengite also occurs in diamond-bearing crustal compositions (Shatsky *et al.*, 1995; Zhang *et al.*, 1997). The coexistence of phengite and phlogopite in marls and impure carbonates has been reported by Dachs (1986, 1990) in the Eastern Alps (Eclogite Zone, Tauern), suggesting a broad zone with two coexisting K-micas between 0·6 and 2·0 GPa at 550–600°C.

The conditions and nature of the reactions that lead to replacement of biotite by phengite with increasing *P* are poorly defined by experiments. Mafic, pelitic, and carbonate-bearing eclogites in nature (Caron & Pequinot, 1986; Sorensen, 1986; Droop *et al.*, 1990; Zhang *et al.*, 1995; Ogasawara *et al.*, 2000) and in experiments conducted above 2·4 GPa on such lithologies have phengite as the principal potassic phase (Massonne & Schreyer, 1987, 1989; Domanik & Holloway, 1996, 2000; Massonne & Spzurka, 1997; Schmidt & Poli, 1998; Hermann & Green, 2001; Schmidt *et al.*, 2004). For carbonate-free pelites, greywackes and basalts, biotite and amphibole are the main reactant phases in fluid-absent melting reactions at pressures below 2·5 GPa (Vielzeuf & Holloway, 1988; Winther & Newton, 1991; Patiño Douce & Beard, 1995; Vielzeuf & Schmidt, 2001; Auzanneau *et al.*, 2006), whereas phengite is the only hydrous phase at pressures between 3 and 8–10 GPa (Domanik & Holloway, 1996; Schmidt, 1996; Ono, 1998; Schmidt *et al.*, 2004). The biotite to phengite reaction thus has major implications for melting in high-*P* environments. Consequently, this study determines the phase relations in carbonate-saturated pelites focusing on (1) the composition and stability of the potassic micas (i.e. the biotite to phengite reaction at subsolidus conditions), and (2) the melting reactions, conditions and melt compositions at pressures in the vicinity of the biotite to phengite reaction.

EXPERIMENTAL METHODS

Experiments were performed in the model system K_2O–CaO–MgO–Al_2O_3–SiO_2–H_2O–CO_2 (KCMASH–CO_2), a simplified system reproducing the mineralogy of carbonate-saturated pelites. The major differences with respect to natural systems are the lack of Fe and Na, whose effect is considered in the Discussion.

Experimental apparatus

Experiments were conducted in an end-loaded 14 mm bore diameter piston cylinder apparatus. Assemblies were composed of an outer NaCl sleeve, a Pyrex glass sleeve, a straight graphite heater, a corundum disc between thermocouple and capsule, and cylinders of crushable MgO inside the furnace. A friction correction of 3% applied to the nominal *P* was obtained by calibration against fayalite + quartz = ferrosilite at 1000°C and 1·41 GPa (Bohlen *et al*, 1980) and against the quartz–coesite transition at 3·07 GPa and 1000°C (Bose & Ganguly, 1995). Hydraulic pressure was maintained by an automatically controlled screw worm jack with a relative precision better than 0·3 bar oil pressure, equivalent to 2·5 MPa sample pressure. Temperature was controlled by a Eurotherm controller within ±2°C using a B-type thermocouple ($Pt_{94}Rh_6$–$Pt_{70}Rh_{30}$), not corrected for the P effect on thermocouple e.m.f. The capsules were centred at the hot spot to within ±0·5 mm, the thermocouple tip thus recording the coldest *T* in the capsule. Thermal gradients were measured in this study to ±10°C for capsules at 2·0 GPa, 1300°C. Below 1000°C, pure gold capsules were used; above 1000°C, $Au_{50}Pd_{50}$ capsules were employed. Capsules were welded at one end, fired, filled with starting material previously dried at 110°C, and then welded shut. A single capsule of 3 mm o.d. (outer diameter) or two capsules (placed side by side) of 2·3 mm o.d. and 3·8 mm length were used. Experiments were quenched by turning off the power to the furnace, resulting in a temperature drop to <200°C within 10 s. Capsules were mounted longitudinally in epoxy and polished to a level at the centre of the capsule.

Starting material

The bulk composition (Table 1) corresponds to a mica-rich marl that yields 20 wt % mica and 4·5 wt % carbonate if all K and CO_2 is stored in micas and carbonates, respectively. The starting material is composed of a synthetic glass made of oxides (SiO_2, Al_2O_3, MgO, CaO) and natural potassic feldspar. The glass was ground to <5 μm in an automatic agate mill under ethanol and then remelted at 1300°C for 45 min using a new Pt-crucible. The milling, grinding and firing was repeated three times to ensure homogeneity of the glass (controlled by microprobe). The glass was then powdered and mixed with $Al(OH)_3$ and $CaCO_3$ to introduce the desired proportions of H_2O and CO_2. Free water or CO_2 was not added, to allow precise control of the amounts of volatiles and to prevent volatile loss during welding. To enhance reaction rates, the composition had ~2 wt % water in excess, relative to the amount of H_2O bound in the expected hydrous phases under subsolidus conditions (biotite, phengite, zoisite and amphibole). Furthermore, most sub- and near-solidus runs were

Table 1: Experimental bulk starting composition (MC) and three comparative natural compositions

	Bulk MC	Ant543*	Frey(78)†	GLOSS‡
SiO_2	51·44	46·57	44·5	58·57
Al_2O_3	21·79	17·99	18·3	11·91
FeO_{tot}	0	7·38	4·8	5·21
MgO	7·36	1·61	2·8	2·48
CaO	11·79	5·45	9·7	5·95
Na_2O	0	1·91	1·4	2·43
K_2O	1·94	2·83	3·4	2·04
H_2O	3·60	11·97	2·8	7·29
CO_2	2·09	3·83	10·7	3·01
Total (wt %)	100·0	99·5	98·4	98·9
Al/(Na + K + 2Ca) molar	0·48	0·69	0·44	0·43
Al/(Na + K) molar	10·38	2·90	3·06	1·92
X_{CO2}§	0·19	0·12	0·61	0·14

*Fe-calcareous claystone (Plank & Langmuir, 1998).
†Calc-schist from Alps (Frey, 1978).
‡Global Subducting Sediment (GLOSS, Plank & Langmuir, 1998).
§Molar $CO_2/(CO_2 + H_2O)$.

saturated in dolomite, to buffer the CO_2 content of the fluid. The bulk composition was chosen to maximize component saturation at sub- or near-solidus conditions; that is, to achieve the highest possible number of saturated phases (with $SiO_2 > Al_2O_3$ resulting in a SiO_2-polymorph and kyanite; Fig. 1). Phase compositions at subsolidus conditions were fully buffered (with respect to the bulk composition).

ANALYTICAL TECHNIQUES

Experimental charges were analysed using a JEOL JXA8200 or a Cameca SX50 electron microprobe using silicate, carbonate, and oxide standards, 15 kV acceleration voltage, and a beam current of 20 nA for silicate minerals and 10 nA for carbonates and glasses. Acquisition times were 10–20 s for all elements, measuring K first (10 s) to avoid alkali loss. A fully focused beam was applied to most water-free crystalline phases, providing totals close to 100 wt %. Because micas, carbonates, quartz/coesite and glasses exhibit electron beam damage at a diameter less than 5 μm, a defocused beam (2–50 μm) was used whenever possible. Textural phase relations were analysed from secondary electron (SE) and back-scattered electron (BSE) images obtained from the microprobes and by scanning electron microscopy (SEM) using a Camscan CS44LB instrument equipped with an energy-dispersive spectrometer (EDS). Polymorphs of phases were identified by micro-Raman spectroscopy using an Ar laser with $\lambda = 488$ nm.

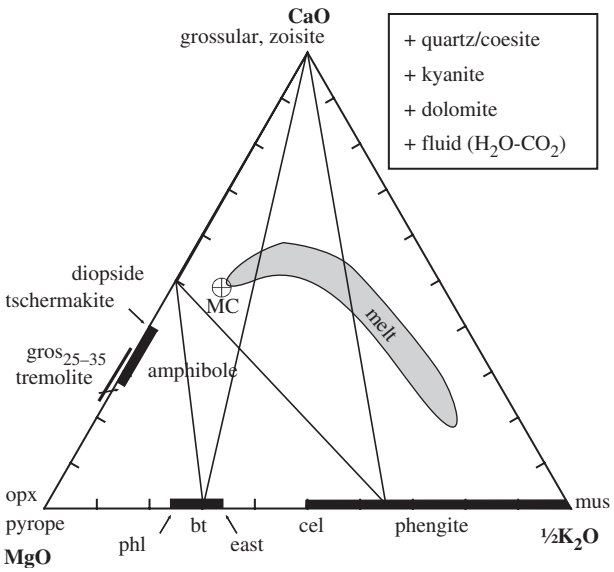

Fig. 1. Composition space and subsolidus chemography of carbonate-saturated pelites in KCMASH–CO_2 saturated with and projected from quartz/coesite + kyanite + dolomite + fluid with the MC starting bulk composition and phase assemblages (fine lines) near the biotite to phengite reaction. Mineral solid solutions are indicated by black bars; the grey field represents the range of experimental melt compositions. Phase abbreviations used throughout this study are: amph, amphibole; bt, biotite; CaTs, Ca-Tschermaks clinopyroxene; cel, MgAl-celadonite; cs, coesite; cor, corundum; cpx, clinopyroxene; dol, dolomite; east, eastonite; gt, garnet; gros, grossular; kfsp, K-feldspar; ky, kyanite; m, (silicate) melt; mus, muscovite; opx, orthopyroxene; phe, phengite; phl, phlogopite; plag, plagioclase; qz, quartz; tc, talc; trem, tremolite; zo, zoisite.

ATTAINMENT OF EQUILIBRIUM AND MASS-BALANCE CALCULATIONS

All runs in this study are synthesis experiments. Generally, samples show textural equilibrium with 120° triple junctions and well-developed crystal shapes. Apart from garnet, which in a few samples exhibits zonation in Ca–Mg content, phases were compositionally homogeneous (for zoned garnets, rim compositions were used for mass balance). Except for two experiments at 850°C, 2·0 and 2·5 GPa, the number of phases does not exceed that permitted by the phase rule, indicating that no metastable phases are present. Regular trends throughout the entire experimental grid of the calculated phase proportions and phase compositions further indicate that equilibrium conditions were reached in most experiments. Two experiments at 750°C, 2·0 and 2·5 GPa remained extremely fine grained, resulting in poor crystallinity and poor analytical conditions, in particular for the micas. However, a few analyses of good quality were obtained for most

phases present. For the experiment at 2·5 GPa and 900°C, the melt composition could not be determined because of fine-grained dispersed kyanite in the melt. Hence, for the five experiments reported here, phase proportions were estimated from BSE images and element distribution maps.

Calculated phase proportions were obtained by a non-weighted least-squares fit, mass balancing the bulk starting composition against averaged mineral phases. Standard deviations of phase proportions were determined by Monte Carlo error propagation from the uncertainties in the phase compositions. At subsolidus conditions, six solid phases and excess fluid were present in our seven-component system (Table 2). Thus, it was necessary to include the fluid in the mass-balance calculations. As the experimental fluid composition was not determined, we selected an X_{CO2} of 0·14, as calculated at 750–850°C along a high-T geotherm (Kerrick & Connolly, 2001) for an average marine sediment bulk composition (GLOSS, Plank & Langmuir, 1998; Table 1). This is comparable with the X_{CO2} of 0·10–0·19 in the fluid of H_2O–CO_2-bearing tholeiitic basalt at 730°C and 2·0 GPa (Molina & Poli, 2000). Extrapolating the values obtained by Molina & Poli (2000) to higher pressures indicates that the X_{CO2} of the fluid decreases with increasing P.

Experiments above the solidus resulted in fewer than six phases (including melt and fluid), and mass-balance calculations were performed without H_2O and CO_2 as fit components. The composition of the fluid coexisting with melt could not be obtained, and thus the solubilities of H_2O and CO_2 in both the melt and fluid remain unknown. Bulk deficiencies in K_2O from mass balance are attributed to the analytical procedure for small glass pools (electron beam damage).

EXPERIMENTAL RESULTS

Phase stabilities

A total of 33 experiments were performed between 2·0 and 3·7 GPa at 750–1300°C (Table 2) allowing us to constrain phase stabilities, devolatilization, and melting reactions (Fig. 2). All experiments above the solidus have rounded vesicles in the glass (e.g. Fig. 3g and h), indicating that fluid was present. Just below the solidus, fluid occurs interstitially between the solid phases (Fig. 3i). Throughout the investigated P–T grid, dolomite constitutes the stable carbonate mineral up to 800°C at 2·3 GPa and up to 950°C at 3·5 GPa. Quartz or coesite are stable to 850°C at 2·0 GPa and to ~1050°C at 3·5 GPa. Between 2·0 and 2·5 GPa, partial melting occurs between 850 and 900°C, whereas at 3·0–3·5 GPa melting occurs at 900–940°C. Zoisite is stable to just above the solidus (i.e. to 900°C at 2·5 GPa and to ~970°C at 3·5 GPa). In this P range, zoisite is the last hydroxyl-bearing phase that is in equilibrium with melt. Clinopyroxene is present in almost all experiments, except at $T \leq 875$°C at 2·0 GPa and $T \leq 750$°C at 2·5 GPa, where it is replaced by amphibole, the latter being restricted to this part of the P–T grid. Garnet emerges between 950 and 1050°C and is stable to 1250–1300°C at 2·5 GPa and to >1300°C at 3·5 GPa. At 2·5 GPa, melt and fluid are the only phases present above 1300°C. Kyanite is almost omnipresent within the P–T diagram except at the highest temperatures at 2·5 GPa, where it is replaced by corundum (at ≥1200°C).

Three experiments contain eight phases (including fluid), indicating that they are situated on a univariant reaction (MC-04 on the amphibole to clinopyroxene reaction, MC-06 on the biotite to phengite reaction, and MC-03 on the solidus). All other subsolidus experiments have seven phases leading to full buffering of the phase compositions, whereas all other supersolidus experiments have six or fewer phases present.

The experiments result in three distinct regions: a phengite and a biotite stability field, separated by a narrow zone at 2·4–2·6 GPa where both micas might coexist, and at higher temperatures a field where micas are replaced by silicate melt (Fig. 3b, d and f–h). Phengite is stable to T <850°C at 2·5 GPa and to T <950°C at 3·5 GPa. In this field, phengite is the only potassic phase present and coexists with clinopyroxene, zoisite, dolomite, kyanite, coesite/quartz and an H_2O–CO_2 fluid (Fig. 3a). At pressures below the biotite to phengite reaction, phengite is absent and several biotite-present stability fields can be determined with slightly different coexisting phase assemblages (Figs 2 and 3c, e). Together, these smaller stability fields constitute the P–T region at ≤850°C, 2·4 GPa.

Phase compositions and textures

Phengites typically form ≤15 μm laths or tabular grains, sometimes clustering in larger aggregates up to 40 μm in size. Not all experiments have grains large enough to be analysed with a defocused beam, introducing the potential for K loss during microprobe analyses. The measured K contents of the phengites, however, indicate less than 3% (relative) K loss (except run MC36 at 3 GPa, 900°C). Phengites in the KCMASH–CO_2 system are mainly a solid solution between muscovite $\ddot{K}Al_2[AlSi_3]O_{10}(OH)_2$ and MgAl-celadonite $\ddot{K}MgAl[Si_4]O_{10}(OH)_2$, the inverse Mg-Tschermak's substitution ($MgSiAl_{-2}$) being the dominant exchange mechanism. For most phengites (Table 3), the sum of cations is close to the 7·0 a.p.f.u. of ideal dioctahedral micas (Velde, 1965). Nevertheless, the Mg content of the phengites, especially at $P \leq 3{\cdot}0$ GPa, is increased with respect to a dioctahedral stoichiometry, by up to 0·2 Mg p.f.u., implying an increased octahedral occupancy (Fig. 4a). This is supported by lower Al_{tot} and Si contents than for ideal phengites (Fig. 4b) and can be attributed to exchange along the di–trioctahedral mica substitution ($Mg_{-3}Al_{2}$) between muscovite and phlogopite. As expected, the Si content in phengite increases with P [i.e. from 3·30 to 3·48 Si p.f.u. at 2·4–3·5 GPa (850°C, Fig. 4c)],

*Table 2: Experimental run conditions and calculated phase proportions (wt %)**

Run no.	*P* (GPa)	*T* (°C)	Time (h)	biotite	phengite	intermediate mica	cpx	zoisite	garnet	glass†	amphibole	dolomite	kyanite	corundum	quartz/coesite	fluid‡ (excess)
MC-05§	2·0	750	88	18	–	–	–	42	–	–	10	3	7	–	18	2
MC-04§	2·0	850	140	9	–	–	22	22	–	10	8	–	15	–	11	3
MC-08	2·0	950	112	–	–	–	48·9 (1·7)	–	–	26·9 (1·9)	–	–	24·2 (1·0)	–	–	present
MC-15	2·0	1050	52	–	–	–	50·6 (2·3)	–	0·3	29·8 (1·9)	–	–	19·3 (1·2)	–	–	present
MC-11	2·3	750	143	20·3	–	–	–	40·3	–	–	10·2	3·1	6·6	–	17·4	2·2
MC-20	2·3	800	166	21·7	–	–	9·9	35·5	–	–	–	2·9	9·7	–	17·6	2·6
MC-12	2·3	850	112	16·2 (1·9)	–	–	25·5 (1·3)	24·8 (2·3)	–	–	–	–	14·8 (1·0)	–	15·4 (1·1)	3·3
MC-13	2·3	900	121	–	–	–	47·8 (1·8)	–	–	25·2 (2·0)	–	–	26·9 (0·7)	–	–	present
MC-22	2·4	750	150	22·7	–	–		42·5	–	–	4·8	3·2	6·6	–	18·1	2·2
MC-17	2·4	800	107	18·8	–	–	13·3	32·6	–	–	–	2·8	11·6	–	18·0	2·9
MC-21	2·4	850	116	–	18·8	–	33·5	12·2	–	–	–	2·6	17·1	–	12·5	3·4
MC-06§	2·5	750	121	9	9	<1	–	32	–	–	18	3	17	–	10	present
MC-24	2·5	800	141	–	18·8	–	32·9	11·7	–	–	–	2·5	18·3	–	12·4	3·4
MC-03§	2·5	850	104	–	12	<1	38	9	–	7	–	2	20	–	9	3·0
MC-38§	2·5	900	285	–	–	–	48	2	–	15	–	–	25	–	10	present
MC-07	2·5	950	107	–	–	–	50·9 (1·4)	–	–	24·6 (2·0)	–	–	24·5 (1·6)	–	–	present
MC-09	2·5	1050	69	–	–	–	46·2 (2·0)	–	0·1	32·4 (1·3)	–	–	21·3 (1·3)	–	–	present
MC-26	2·5	1100	88	–	–	–	45·0 (1·7)	–	4·3 (2·1)	33·3 (1·1)	–	–	17·4 (1·0)	–	–	present
MC-27	2·5	1200	74	–	–	–	10·6 (1·4)	–	16·3 (1·7)	71·4 (1·5)	–	–	–	1·7 (0·3)	–	present
MC-31	2·5	1250	85	–	–	–	–	–	23·2 (0·8)	76·8 (0·8)	–	–	–	<1	–	present
MC-35	2·5	1300	87	–	–	–	–	–	–	100·0 (1·3)	–	–	–	–	–	present
MC-16	2·7	800	184	–	18·2	–	33·7	11·5	–	–	–	2·5	18·5	–	12·3	3·4
MC-25	2·7	850	116	–	18·4	–	35·7	10·9	–	–	–	2·5	17·6	–	11·6	3·4
MC-01	3·0	850	129	–	18·1	–	36·0	10·3	–	–	–	2·5	18·3	–	11·3	3·5
MC-36	3·0	900	121	–	17·4	–	38·0	8·0	–	–	–	2·4	19·2	–	11·4	3·6
MC-18	3·0	950	172	–	–	–	43·0	–	–	19·8	–	1·2	27·7	–	6·0	present
MC-02	3·5	850	117	–	17·5	–	36·7	8·9	–	–	–	2·4	20·4	–	10·7	3·5
MC-23	3·5	950	68	–	–	–	49·9	1·6	–	23·8	–	–	24·5	–	0·3	present
MC-28	3·5	1150	68	–	–	–	35·2 (1·7)	–	11·2 (1·9)	35·8 (0·6)	–	–	17·9 (0·7)	–	–	present
MC-29	3·5	1200	90	–	–	–	10·0 (2·3)	–	29·2 (1·9)	51·1 (1·1)	–	–	9·7 (0·6)	–	–	present
MC-30	3·5	1250	96	–	–	–	–	–	31·8 (1·0)	62·3 (0·8)	–	–	5·9 (0·4)	–	–	present
MC-34	3·5	1300	71	–	–	–	–	–	21·5 (1·2)	72·2 (1·1)	–	–	6·3 (0·5)	–	–	present
MC-37	3·7	1100	146	–	–	–	49·1 (2·6)	–	2 (1·0)	27 (1·3)	–	–	23 (1·2)	–	–	present

*Values in parentheses are 1 SD (in wt %). For experiments with six phases and excess fluid, standard deviations cannot be calculated.
†For experiments with glass (melt) and fewer than six phases, phase proportions are calculated on a fluid-free basis.
‡For melting experiments, fluid composition and proportion is not determined, as H_2O and CO_2 solubility for the melts are undetermined.
§Estimated weight proportions from BSE images, fitted by recalculation of phase compositions and estimated proportions to bulk composition.

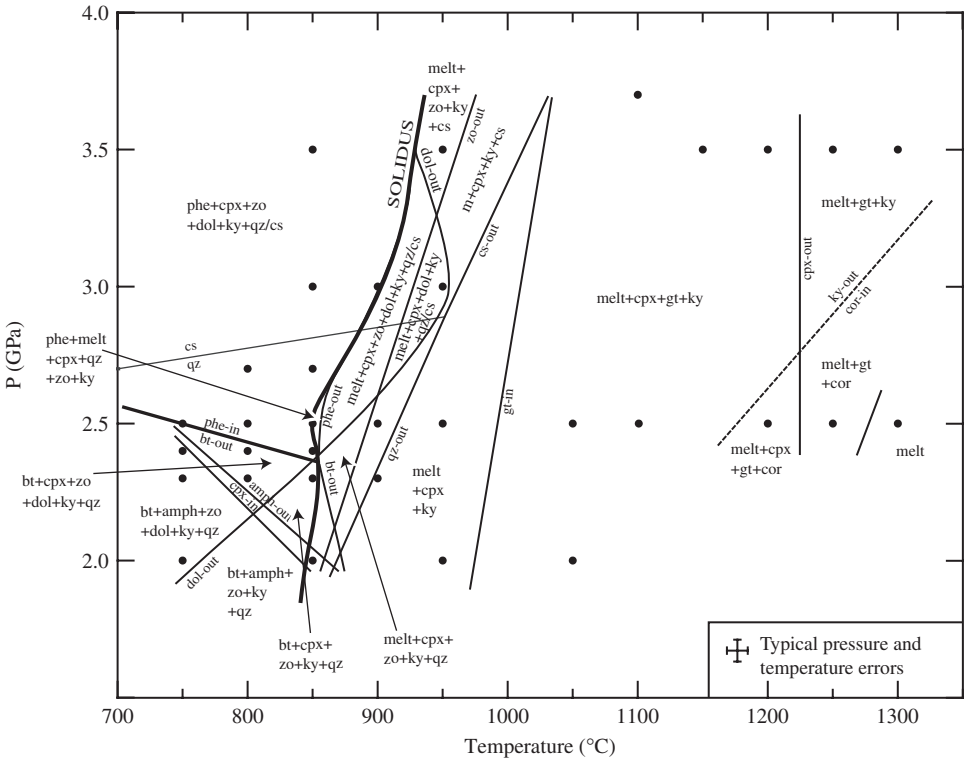

Fig. 2. Experimental pressure–temperature diagram for the simplified carbonated pelite composition MC in KCMASH–CO_2. The bold continuous line is the experimentally determined solidus, and points indicate experiments. Quartz–coesite transformation from Bose & Ganguly (1995).

and Al_{tot} p.f.u. decreases with increasing *P*. This trend is qualitatively coherent with previous results from the KMASH (Massonne & Schreyer, 1987) and KCMASH systems (Hermann, 2002), and for phengites in general (Velde, 1965, 1966, 1967; Guidotti & Sassi, 1998, 2002). The difference in the location and slope of the Si-isopleths in phengite for the different systems reflects the different buffering phase assemblages, or, in their absence, the various bulk compositions.

Similar to phengite, biotite forms small (≤15 μm) laths. The compositions of biotites (Table 3) are more scattered than for phengites, reflecting poor analytical conditions. In a KCMASH–CO_2 system, ideal biotite results from Mg-Tschermak's substitution ($Mg_{-1}Si_{-1}Al_2$) within the solid solution phlogopite–eastonite; that is, $KMg_3[AlSi_3]O_{10}(OH)_2$–$KMg_2Al[Al_2Si_2]O_{10}(OH)_2$. However, the sum of cations for our biotites varies between 7·35 and 7·66 a.p.f.u. with octahedral occupancies from 2·55 to 2·82 p.f.u. and interlayer cation vacancies of 0·11–0·28 p.f.u., suggesting non-ideal biotites with a cation-deficient interlayer and an octahedral vacancy of 0·18–0·45 p.f.u. (Fig. 4a). With increasing *P* and decreasing *T*, potassium contents decrease concomitant with an increase in silica contents, exceeding the upper limit of 3·0 Si p.f.u. for ideal phlogopites. This results in a biotite stoichiometry, which can be understood as a complex solid solution between ideal biotite and phengite, combined with a talc $Mg_3[Si_4]O_{10}(OH)_2$ component (Fig. 4b and d). This complex substitution mechanism with *P* has been suggested by Wunder & Melzer (2002) and Hermann (2002), and discussed by Comodi *et al.* (2004) for high-*P* biotites. Despite our limited *P*–*T* range yielding biotites, this tendency is confirmed: the lowest Si content (2·99 Si p.f.u.) is observed at 2·0 GPa (850°C) increasing to 3·20 Si p.f.u. at 2·4 GPa (750°C).

Rare intermediate mica compositions between biotite and phengite, in part with a considerable talc component (Table 3) are observed at 2·5 GPa (i.e. close to the biotite to phengite reaction). This suggests either the stable existence of such micas or polysomatic series, or extremely fine intergrowths of biotite and phengite. To our knowledge such micas have not been observed in nature, and in several other experimental studies at the upper *P* stability of biotite (Green & Hellman, 1982; Massone & Schreyer, 1987; Hermann & Green, 2001; Auzanneau *et al.*, in preparation), and this transient feature has not been investigated further.

Clinopyroxene forms compositionally homogeneous, ≤20 μm tabular to prismatic grains. At subsolidus conditions, abundances of clinopyroxene and zoisite are inversely proportional, clinopyroxene dominating at higher pressures

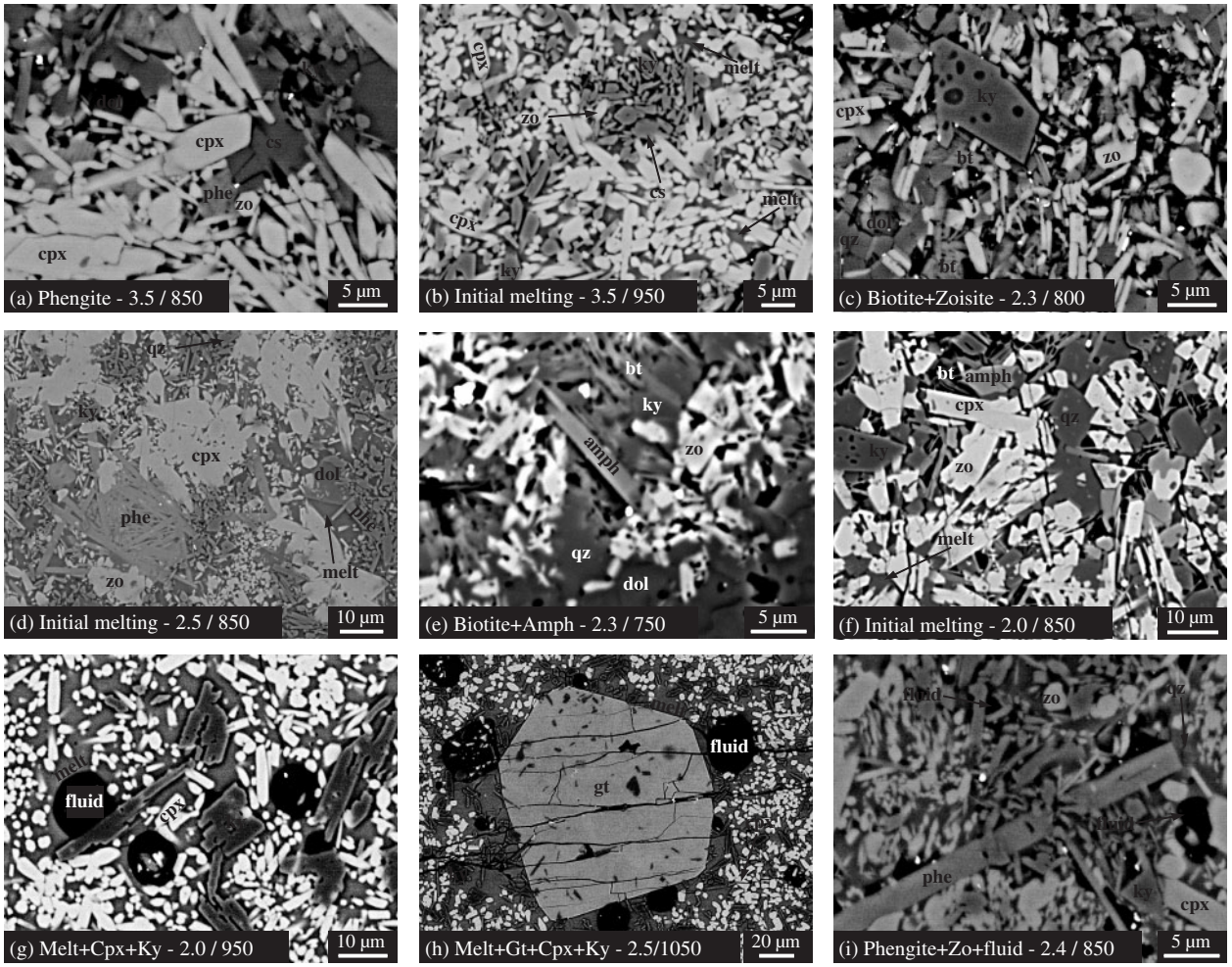

Fig. 3. BSE images of run products (P in GPa/T in°C). (a) Phengite stability field, (b) lowest temperature melting at 3·5 GPa, (c) biotite + zoisite stability field, (d) first melt at 2·5 GPa coexisting with phengite, (e) biotite + amphibole stability field, (f) melt + biotite + amphibole + clinopyroxene at 2·0 GPa and 850°C; (g) round fluid bubbles in the melt + clinopyroxene + kyanite stability field and (h) in the melt + garnet + clinopyroxene + kyanite stability field; (i) small interstitial pockets of fluid coexisting with phengite and zoisite at 2·4 GPa and 850°C; the matrix is composed of quartz.

and temperatures. Clinopyroxenes contain low contents of K_2O (<0·37 wt %), indicating insignificant incorporation of K^+ at the investigated pressures. The normalization scheme employed (Cawthorn & Collerson, 1974) allows for octahedral M2-site vacancies, representing clinopyroxene as a quaternary solid solution between diopside ($CaMg[Si_2]O_6$), clinoenstatite (C-en, $Mg_2[Si_2]O_6$), Ca-tschermakite (CaTs; $CaAl[AlSi]O_6$), and Ca-eskolaite (Ca-esk; $Ca_{0.5}\square_{0.5}Al[Si_2]O_6$) (Fig. 5a). Compositionally, the clinopyroxenes are Al-rich diopsides (Table 4) with Al_2O_3 contents increasing with T from 4–5 wt % at 800–850°C to almost 17 wt % at 1200°C (2·5 GPa). Above the solidus, Si and Mg contents decrease with T, whereas Al increases on the tetrahedral site from 0·01 Al p.f.u. at 850°C to 0·30 Al p.f.u. at 1200°C, suggesting an increase of the Tschermak's component ($Mg_{-1}Si_{-1}Al_2$) with T (Fig. 5a). Calculated M2-site vacancies are up to 0·03–0·08 p.f.u. corresponding to 6·3–16·2 mol % Ca-eskolaite, increasing with P (at constant T). Experimental clinopyroxenes with 4–9 mol % Ca-eskolaite (at 3·5–7·5 GPa and 740–1180°C) have been reported by Schmidt *et al.* (2004) in a pelite and a greywacke bulk composition. For a KCMASH composition, Hermann (2002) reported Ca-eskolaite contents up to 10 mol % at 4·5 GPa and 1100°C, based on a correlation of cation totals with excess Al on the M1 site, as observed in this study. In the experiments by Konzett *et al.* (2008) on natural and synthetic eclogites containing garnet + clinopyroxene + quartz/coesite ± TiO_2 ± kyanite, Ca-eskolaite amounted to 4–18 mol % at 2·5–11 GPa and 850–1350°C, mainly increasing with T. Absolute Ca-eskolaite contents in clinopyroxenes from this study (Hermann, 2002; Schmidt *et al.*, 2004), and in natural clinopyroxenes from high-P terranes

*Table 3: Compositions of micas**

	Phengites							
P(GPa)/*T*(°C):	2·4/850	2·5/800	2·5/850	2·7/800	2·7/850	3·0/850	3·0/900	3·5/850
No. of analyses:	9	9	16	9	8	17	6	24
SiO_2	49·51 (0·95)	50·71 (1·14)	49·95 (1·46)	50·03 (0·97)	50·60 (0·87)	51·36 (0·78)	48·88 (1·09)	52·52 (0·87)
Al_2O_3	27·38 (1·36)	27·69 (1·00)	27·94 (1·64)	27·68 (0·41)	28·68 (0·65)	28·28 (0·66)	24·29 (1·11)	26·12 (0·89)
MgO	7·04 (0·39)	5·75 (0·43)	6·75 (0·63)	5·87 (0·43)	5·21 (0·24)	5·04 (0·20)	4·78 (0·41)	4·99 (0·32)
CaO	0·31 (0·09)	0·64 (0·48)	0·29 (0·30)	0·24 (0·12)	0·22 (0·09)	0·25 (0·19)	1·75 (0·75)	0·20 (0·11)
K_2O†	10·21 (0·52)	10·26 (0·32)	10·49 (0·58)	10·54 (0·28)	10·50 (0·25)	10·42 (0·68)	10·61 (0·36)	10·83 (0·31)
H_2O (calc)	4·49 (0·03)	4·53 (0·04)	4·54 (0·04)	4·49 (0·04)	4·54 (0·02)	4·56 (0·06)	4·27 (0·05)	4·52 (0·02)
Total	98·96 (0·53)	99·59 (0·73)	99·95 (0·70)	98·86 (0·73)	99·76 (0·42)	99·91 (0·83)	94·58 (1·01)	99·17 (0·38)
Si	3·303 (66)	3·354 (60)	3·307 (80)	3·338 (40)	3·338 (42)	3·378 (23)	3·435 (44)	3·485 (52)
Al^{IV}	0·697 (66)	0·646 (60)	0·693 (80)	0·662 (39)	0·662 (42)	0·622 (81)	0·565 (45)	0·515 (52)
Al^{VI}	1·456 (45)	1·513 (41)	1·478 (67)	1·516 (22)	1·569 (21)	1·571 (97)	1·446 (73)	1·528 (28)
Mg	0·700 (41)	0·567 (46)	0·666 (65)	0·584 (44)	0·512 (24)	0·494 (15)	0·501 (49)	0·493 (32)
Ca	0·022 (6)	0·046 (34)	0·023 (22)	0·017 (8)	0·016 (7)	0·017 (13)	0·132 (58)	0·014 (8)
K	0·869 (47)	0·865 (27)	0·881 (52)	0·897 (27)	0·884 (23)	0·875 (67)	0·951 (32)	0·916 (29)
H	2·000	2·000	2·000	2·000	2·000	2·000	2·000	2·000
Total cations	7·048 (43)	6·991 (37)	7·047 (56)	7·014 (24)	6·981 (28)	6·957 (44)	7·031 (55)	6·951 (31)
Oct. vacancy‡	0·843	0·919	0·856	0·900	0·918	0·935	1·012	0·979

	Biotites						Intermediate mica	
P(GPa)/*T*(°C):	2·0/850	2·3/750	2·3/800	2·3/850	2·4/750	2·4/800	2·5/750	2·5/850
No. of analyses:	4	2	4	17	3	10	2	2
SiO_2	43·44 (0·84)	44·48	46·86 (1·35)	42·97 (1·21)	47·16 (0·79)	44·81 (1·06)	50·57	46·83
Al_2O_3	18·42 (1·47)	16·38	17·45 (0·25)	19·53 (0·95)	16·00 (0·70)	17·46 (0·49)	22·65	21·75
MgO	22·73 (1·26)	19·16	21·81 (0·48)	19·03 (0·91)	22·50 (0·62)	21·73 (0·51)	9·50	15·30
CaO	0·28 (0·09)	0·30	0·37 (0·12)	0·25 (0·23)	0·51 (0·20)	0·26 (0·17)	2·04	0·40
K_2O†	9·93 (0·27)	8·86	8·91 (0·50)	9·63 (0·32)	8·29 (0·51)	10·12 (1·11)	8·54	10·44
H_2O (calc)	4·35 (0·02)	4·26	4·45 (0·06)	4·24 (0·06)	4·42 (0·04)	4·35 (0·03)	4·44	4·42
Total	99·14 (0·42)	93·43	99·86 (1·09)	95·64 (1·18)	98·89 (0·28)	98·73 (0·53)	97·72	99·12
Si	2·991 (46)	3·194	3·154 (58)	3·070 (75)	3·197 (102)	3·085 (61)	3·412	3·180
Al^{IV}	1·009 (26)	0·806	0·846 (58)	0·930 (75)	0·846 (58)	0·915 (61)	0·588	0·820
Al^{VI}	0·486 (84)	0·518	0·539 (31)	0·657 (36)	0·539 (31)	0·503 (31)	1·212	0·920
Mg	2·332 (121)	2·033	2·188 (59)	2·004 (48)	2·274 (85)	2·230 (55)	0·957	1·549
Ca	0·021 (7)	0·023	0·027 (9)	0·028 (23)	0·037 (15)	0·019 (12)	0·147	0·029
K	0·819 (26)	0·775	0·765 (18)	0·862 (8)	0·717 (51)	0·889 (101)	0·734	0·904
H	2·000	2·000	2·000	2·000	2·000	2·000	2·000	2·000
Total cations	7·658 (19)	7·348	7·520 (54)	7·551 (47)	7·610 (95)	7·642 (85)	7·051	7·402
Oct. vacancy‡	0·182	0·449	0·273	0·339	0·251	0·267	0·831	0·531

*Based on 11 oxygens and 2 (OH). Values in parentheses are 1 SD in terms of last digit(s).
†K_2O content adjusted for K loss. Calculated from mass-balanced proportions and bulk K_2O to achieve minimum residuals.
‡Octahedral site vacancy calculated as: vacancy$^{VI} = 7 - (Si + Al + Mg)$ per 11 oxygens formula unit.

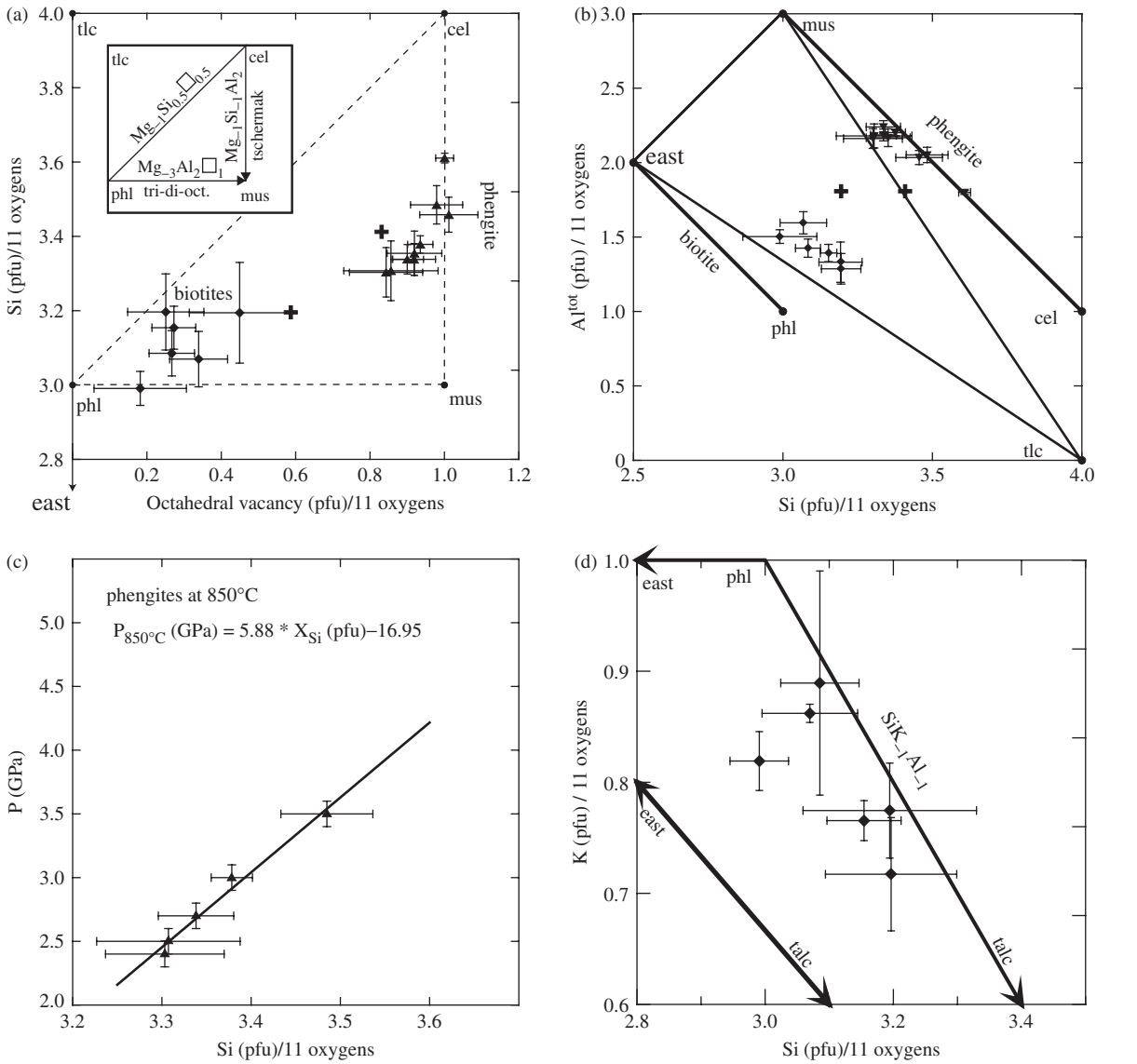

Fig. 4. Composition of experimental biotites and phengites normalized for 11 oxygens. (a) Octahedral vacancy vs Si diagram shows the relation between phengite and biotite in terms of Tschermaks and di–trioctahedral exchange vectors (inset). (b) Si vs Al_{tot} diagram illustrating the close to ideal phengites and the non-ideal trioctahedral biotite. The net substitution vector between the biotites and phengites from each side of the mica reaction is calculated to $Mg_{1·54}Si_{-0·23}Al_{-0·69}\square_{-0·61}$. (c) At 850°C, Si in phengite increases with pressure. (d) Decreasing K with increasing Si content indicates solid solution of biotite towards talc. ◆, biotites; ▲, phengites; +, transitional micas.

(15–20% at 5·0 GPa and 1100°C, Schultze *et al.*, 2000; 8% at >3·3 GPa and 850°C, Schmädicke & Müller, 2000; 12% at 4·5 GPa, 950°C, Katayama *et al.*, 2000) are comparable. Nevertheless, in this study, the maximum Ca-eskolaite content at constant *P* is not attained at the highest temperatures as found by Hermann (2002) and Schmidt *et al.* (2004), but at near-solidus temperatures (850–950°C) (Fig. 5a) similar to the experiments of Pertermann & Hirschmann (2003) at 3·0 GPa on quartz eclogites. Above the solidus, the Ca-eskolaite content in our clinopyroxenes is nearly constant (at 2·0 GPa) or decreases slightly with increasing *T* (at 2·5 and 3·5 GPa).

Amphibole forms ≤20 μm laths or tabular grains occasionally including quartz and kyanite. The analysed amphiboles (Table 5) contain 1·77–1·87 Ca p.f.u., 7·1–7·5 Si p.f.u., and are magnesio- to tremolitic hornblendes exhibiting Tschermak's substitution and some minor $Ca_{-1}Mg$ substitution. In the poorly developed amphibole grains in the run at 750°C and 2·5 GPa, close intergrowth with clinopyroxene is inferred from measured compositions between amphibole and clinopyroxene.

Garnet is generally idiomorphic, varies from <5 to 100 μm in size, and often contains inclusions of kyanite and quartz/coesite. In most experiments, garnets are

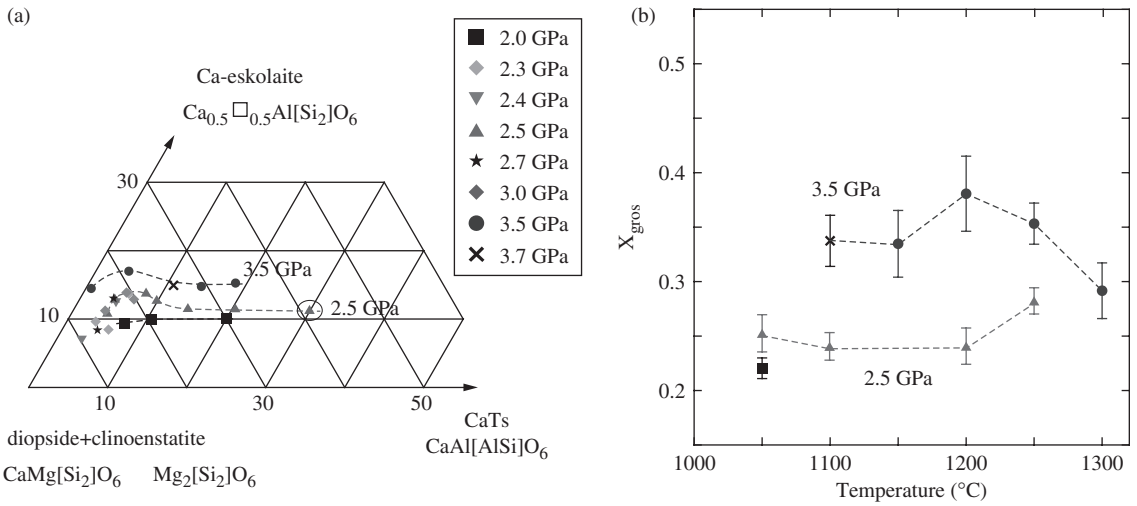

Fig. 5. (a) Clinopyroxene compositions in terms of diopside, clinoenstatite, Ca-Tschermak (CaTs) and Ca-eskolaite. Ca-Tschermak's component increases with temperature and Ca-eskolaite with pressure. For a constant pressure, the maximum Ca-eskolaite content is reached at near-solidus temperatures. A typical standard deviation is given by the ellipse surrounding the point closest to the Ca-Tschermak's apex. (b) Garnet compositions: grossular contents increase with pressure. Dotted lines denote isobaric conditions.

compositionally homogeneous, and display a systematic increase in grossular content (from 22 to 46 mol %; Table 7) with P, but no significant change with T (Fig. 5b).

Zoisite forms ≤20 μm prismatic or tabular grains often comprising small inclusions of clinopyroxene, mica or incompletely reacted starting material. No significant systematic compositional changes are detected. Careful analyses of large homogeneous grains reveal up to 1 wt % MgO, equivalent to 0·13 Mg p.f.u. in the zoisite structure (Table 7). The identification of zoisite (with respect to clinozoisite) was confirmed by micro-Raman spectroscopy, and agrees with the report by Poli & Schmidt (1998, 2004) and Brunsmann *et al.* (2002) of zoisite as the high-P polymorph stable to 7 GPa at 1070°C in the CASH system.

Dolomite forms ≤10 μm subidiomorphic grains with $X_{Mg} = 0{\cdot}46$–$0{\cdot}49$; that is, slightly more calcic than an ideal composition (Table 7), comparable with the dolomites described by Luth (1995).

Kyanite, quartz/coesite and corundum are pure in composition, generally forming ≤25 μm laths, tabular, or prismatic grains, often with irregular inclusions of all other phases present in the phase assemblage as well as of incompletely reacted starting material. Corundum is a product of incongruent melting of kyanite.

The first glass (quenched melt) is observed in small interstitial pools less than 5–10 μm in size. At all pressures investigated, clinopyroxene, kyanite and quartz coexist with the lowest-T melts. At 2·0 GPa further coexisting phases are biotite, amphibole and zoisite, at 2·5 GPa phengite, zoisite and dolomite, at 3·0 GPa dolomite, and at 3·5 GPa zoisite. The initial melts are relatively rich in K_2O (9–11 wt %) and SiO_2 (71–74 wt %), but low in CaO (2–4 wt %) and MgO (<1 wt %) (Table 6). They are metaluminous [Al/(K + 2Ca) = 0·66–0·98] granitic melts with a Al/K of 1·0–1·4 (Fig. 6), reflecting the dominance of mica + quartz/coesite in the solidus reactions. Within a T increase of 100–250°C above the solidus, melts become enriched in Mg, Ca, and Al, as a result of melting of clinopyroxene and kyanite, producing slightly peraluminous or metaluminous [Al/(K + 2Ca) = 0·98–1·04] granitic melts. Further T increase results in garnet crystallization and metaluminous melts with Al/(K + 2Ca) ratios near 0·9 at 2·5 GPa and of 0·7–0·75 at 3·5 GPa, representing granodioritic to tonalitic melts at 2·5 GPa, and quartz-monzonitic melts at 3·5 GPa.

All supersolidus experiments contain large vesicles of 5–40 μm in diameter (Fig. 3 g and h). Using SEM, quench phases precipitated in the vesicles can be observed, indicating that these vesicles represented bubbles filled with solute-rich fluid during the experiments.

DISCUSSION OF PHASE RELATIONS AND ABUNDANCES

Phase proportions across the biotite to phengite reaction in a nearly isothermal subsolidus section at 750–850°C, and along isobaric sections at 2·5 and 3·5 GPa are presented in Fig. 7. We first discuss the biotite to phengite and amphibole to clinopyroxene subsolidus reactions, and then melting reactions. Reactions (1)–(5) are calculated in molar coefficients from phase compositions near the reaction, with melt normalized to eight oxygens. The low-variance reactions (6) and (7) are calculated from the differences in phase abundances between two experiments. Reactions are balanced without dolomite and the CO_2 component in melt and fluid, as the latter two are not directly

*Table 4: Clinopyroxene composition**

P(GPa)/*T*(°C):	2·0/850	2·0/950	2·0/1050	2·3/800	2·3/850	2·3/900	2·4/850	2·4/800	2·5/800	2·5/850	2·5/900	2·5/950	2·5/1050
No. of analyses:	8	10	7	16	14	7	8	14	6	30	5	22	22
SiO_2	53·67 (0·72)	53·10 (1·23)	50·55 (0·75)	54·43 (0·44)	54·26 (0·68)	54·28 (0·77)	54·55 (0·62)	54·04 (0·51)	54·72 (0·80)	54·56 (0·90)	53·29 (0·46)	52·94 (1·06)	51·79 (0·79)
Al_2O_3	5·91 (0·58)	7·63 (1·04)	12·18 (0·53)	4·15 (0·40)	6·18 (1·35)	5·02 (1·09)	5·51 (0·83)	4·83 (1·04)	3·50 (0·53)	5·32 (1·28)	7·23 (0·62)	7·92 (1·39)	9·71 (0·95)
MgO	16·30 (0·36)	15·95 (0·79)	15·06 (0·36)	16·50 (0·43)	15·80 (0·79)	16·50 (0·51)	15·91 (0·56)	16·37 (0·84)	17·15 (0·45)	15·91 (0·59)	15·16 (0·29)	15·19 (0·73	15·08 (0·63)
CaO	23·78 (0·37)	23·42 (0·43)	22·08 (0·31)	24·19 (0·42)	23·35 (0·84)	24·31 (0·54)	23·76 (0·57)	23·44 (0·38)	24·15 (0·34)	23·74 (0·52)	23·11 (0·24)	23·01 (0·57)	22·83 (0·44)
K_2O	0·08 (0·03)	0·13 (0·08)	0·19 (0·10)	0·06 (0·34)	0·07 (0·04)	0·14 (0·09)	0·18 (0·14)	0·08 (0·03)	0·25 (0·07)	0·07 (0·05)	0·15 (0·09	0·21 (0·15)	0·08 (0·04)
Total (wt %)	99·84 (0·58)	100·23 (0·37)	100·06 (0·65)	99·89 (0·58)	99·74 (0·52)	100·24 (0·53)	99·90 (0·35)	99·06 (0·34)	99·78 (0·69)	99·60 (0·60)	98·94 (0·16)	99·27 (0·34)	99·51 (0·54)
Si	1·921 (17)	1·889 (45)	1·796 (21)	1·959 (25)	1·937 (26)	1·937 (23)	1·947 (27)	1·951 (20)	1·963 (24)	1·952 (32)	1·917 (20)	1·898 (37)	1·852 (29)
Al^{IV}	0·079	0·111	0·204	0·041	0·063	0·063	0·053	0·049	0·037	0·048	0·083	0·102	0·148
Al^{VI}	0·171	0·209	0·307	0·135	0·197	0·148	0·179	0·157	0·111	0·176	0·223	0·233	0·262
Mg	0·870 (14)	0·846 (44)	0·797 (21)	0·885 (18)	0·841 (43)	0·877 (23)	0·846 (27)	0·881 (43)	0·917 (21)	0·848 (32)	0·813 (14)	0·812 (38)	0·804 (31)
Ca	0·912 (17)	0·893 (17)	0·840 (12)	0·932 (14)	0·893 (32)	0·929 (17)	0·908 (20)	0·907 (14)	0·928 (11)	0·910 (21)	0·891 (10)	0·884 (22)	0·875 (17)
K	0·004 (2)	0·006 (4)	0·009 (4)	0·003 (2)	0·003 (2)	0·006 (4)	0·008 (6)	0·004 (2)	0·012 (3)	0·003 (2)	0·007 (4)	0·010 (7)	0·004 (2)
Total cations	3·956	3·954	3·953	3·955	3·934	3·961	3·941	3·948	3·969	3·938	3·934	3·939	3·945
Oct. vacancy†	0·044	0·046	0·047	0·045	0·066	0·039	0·059	0·052	0·031	0·062	0·066	0·061	0·055
Ca-esk (mol %)	8·8	9·3	9·4	9·0	13·1	7·8	11·7	10·4	6·3	12·5	13·3	12·2	11·1

P(GPa)/*T*(°C):	2·5/1100	2·5/1200	2·7/800	2·7/850	3·0/850	3·0/900	3·0/950	3·5/850	3·5/950	3·5/1150	3·5/1200	3·7/1100
No. of analyses:	13	13	8	35	22	6	19	7	16	7	17	14
SiO_2	50·00 (0·64)	47·43 (1·02)	54·03 (0·74)	54·68 (0·90)	54·59 (1·14)	54·21 (0·72)	53·63 (0·85)	55·48 (0·65)	54·68 (0·96)	51·49 (0·42)	50·63 (0·66)	52·70 (0·62)
Al_2O_3	12·56 (1·09)	16·98 (1·27)	4·26 (0·86)	5·36 (1·49)	4·78 (1·57)	6·08 (1·15)	6·48 (0·78)	3·92 (0·87)	6·41 (1·88)	10·46 (0·44)	12·56 (1·05)	8·87 (0·41)
MgO	13·97 (0·68)	12·54 (0·63)	16·63 (0·63)	16·18 (0·83)	16·28 (0·81)	15·54 (0·82)	15·18 (0·39)	16·05 (0·43)	15·23 (1·27)	14·20 (0·29)	13·30 (0·62)	14·83 (0·30)
CaO	22·56 (0·39)	22·45 (0·35)	24·10 (0·49)	23·25 (0·94)	23·90 (0·69)	23·45 (0·98)	23·88 (0·77)	23·83 (0·45)	22·63 (1·88)	22·63 (0·28)	22·88 (0·23)	22·68 (0·29)
K_2O	0·16 (0·14)	0·06 (0·02)	0·08 (0·04)	0·18 (0·11)	0·11 (0·09)	0·15 (0·12)	0·12 (0·11)	0·09 (0·03)	0·37 (0·35)	0·07 (0·02)	0·06 (0·02)	0·12 (0·09)
Total (wt %)	99·38 (0·26)	99·46 (0·65)	99·09 (0·49)	99·64 (0·61)	99·65 (0·70	99·48 (0·41)	99·47 (0·54)	99·38 (0·28)	99·56 (0·41)	99·06 (0·86)	99·42 (0·40)	99·39 (0·54)
Si	1·793 (23)	1·697 (34)	1·950 (27)	1·953 (33)	1·955 (35)	1·941 (26)	1·927 (28)	1·988 (25)	1·954 (44)	1·851 (10)	1·810 (21)	1·887 (19)
Al^{IV}	0·207	0·303	0·050	0·047	0·045	0·059	0·073	0·012	0·046	0·149	0·190	0·113
Al^{VI}	0·324	0·414	0·131	0·179	0·156	0·198	0·201	0·154	0·224	0·294	0·339	0·261
Mg	0·747 (36)	0·669 (33)	0·894 (33)	0·861 (41)	0·869 (45)	0·829 (44)	0·813 (29)	0·857 (22)	0·811 (65)	0·761 (13)	0·709 (32)	0·792 (16)
Ca	0·867 (15)	0·861 (13)	0·932 (17)	0·890 (33)	0·917 (28)	0·900 (41)	0·919 (30)	0·915 (16)	0·866 (71)	0·871 (4)	0·876 (11)	0·870 (11)
K	0·007 (6)	0·003 (1)	0·004 (2)	0·008 (5)	0·005 (5)	0·007 (6)	0·006 (5)	0·004 (1)	0·017 (16)	0·003 (1)	0·003 (1)	0·005 (4)
Total cations	3·945	3·946	3·961	3·938	3·947	3·934	3·939	3·931	3·919	3·929	3·927	3·929
Oct. vacancy†	0·055	0·054	0·039	0·062	0·053	0·066	0·061	0·069	0·081	0·071	0·073	0·071
Ca-esk (mol %)	11·01	10·81	7·78	12·38	10·61	13·22	12·25	13·86	16·17	14·16	14·67	14·30

*Based on 12 charges (Cawthorn & Collerson, 1974). Values in parentheses are 1 SD in terms of last digit(s) (cations).
†Octahedral site vacancy (p.f.u.) calculated as 4 – total cations.

*Table 5: Amphibole compositions**

P(GPa)/*T*(°C):	2·0/750	2·0/850	2·3/750	2·4/750
No. of analyses:	4	16	10	4
SiO_2	53·42 (2·18)	51·99 (0·79)	54·29 (0·99)	54·90 (0·70)
Al_2O_3	9·74 (1·99)	11·65 (0·88)	7·52 (0·94)	7·59 (0·77)
MgO	20·07 (1·40)	20·48 (0·55)	21·27 (0·55)	20·65 (0·85)
CaO	12·26 (1·05)	12·15 (0·46)	12·29 (0·56)	12·39 (0·75)
K_2O	0·34 (0·03)	1·14 (0·30)	0·63 (0·18)	0·64 (0·30)
H_2O (calc)	2·18 (0·01)	2·20 (0·01)	2·18 (0·01)	2·19 (0·02)
Total (wt %)	98·00 (0·19)	99·61 (0·47)	98·17 (0·52)	98·34 (0·79)
Si	7·341 (269)	7·081 (89)	7·496 (126)	7·522 (98)
Al^{IV}	0·659	0·919	0·504	0·478
Al^{VI}	0·920	0·952	0·662	0·757
Mg	4·110 (285)	4·157 (109)	4·397 (124)	4·186 (159)
Ca	1·805 (160)	1·772 (71)	1·767 (69)	1·868 (103)
K	0·059 (5)	0·198 (51)	0·128 (27)	0·087 (53)
H	2·000	2·000	2·000	2·000
Total (p.f.u.)	14·894 (137)	15·080 (57)	14·953 (101)	14·899 (61)

*Based on 46 charges. Values in parentheses are 1 SD in terms of last digit(s).

constrained by the experiments. Furthermore, reactions including melt are mass balanced on a volatile-free basis as we did not quantify volatile contents in the melts.

The pressure-dependent reaction of biotite to phengite

The biotite to phengite reaction is a key reaction in any crustal K-rich lithology and has major implications for the melting behaviour in subduction zones. Micas are among the first minerals that disappear through melting and host many key trace elements and isotopes such as K, Rb, Ba, Sr, B, Pb, and ^{10}Be (Domanik *et al.*, 1993; Ishikawa & Nakamura, 1994; Plank & Langmuir, 1998). In this study, we have constrained the reaction from biotite to phengite to take place over the *P* range 2·4–2·6 GPa at 750–850°C (Figs 2 and 7a). Across the biotite to phengite reaction, the proportions of zoisite + quartz/coesite decrease and those of clinopyroxene + kyanite increase, whereas the sum of biotite + phengite remains almost unchanged and close to the expected 20 wt %. This suggests a K_2O-conservative reaction buffered by zoisite, quartz/coesite, clinopyroxene and kyanite. The stoichiometry of this reaction is calculated from phase compositions just within the stability field of phengite (at 2·7 GPa) and biotite (at 2·3 GPa) at 800 and 850°C to

$$1{\cdot}00\ \text{bt} + 0{\cdot}86\ \text{zo} + 1{\cdot}95\ \text{qz}\ (+\text{dol}) = 1{\cdot}00\ \text{phe} + 1{\cdot}83\ \text{cpx} + 0{\cdot}75\ \text{ky} + 0{\cdot}43\ H_2O\ (+CO_2). \quad (1)$$

Reaction (1) necessarily preserves K_2O as no other K-bearing phase is observed, but somewhat surprisingly, reaction (1) is not H_2O conservative. The amount of fluid (0·5 wt % H_2O in our experiments) produced from zoisite may cause a decrease of the X_{CO2} in the fluid, and/or some concomitant dolomite decarbonation; however, the latter is within error of the mass-balance calculations. Schreinemaker's analysis (see below) indicates that dolomite is a reactant of reaction (1). A decrease of the X_{CO2} in the fluid with increasing *P* was also calculated by Molina & Poli (2000), and corresponds to a decreasing abundance of hydrates and an increase of carbonates in the solid assemblage.

The breakdown reaction of amphibole to clinopyroxene

Amphibole is stable below 875°C, 2·0 GPa and 740°C, 2·5 GPa. To higher pressures and temperatures, the calculated devolatilization reaction

$$1{\cdot}00\ \text{amph} + 1{\cdot}25\ \text{zo} + 0{\cdot}76\ \text{qz}\ (+\text{dol}) = 4{\cdot}70\ \text{cpx} + 2{\cdot}40\ \text{ky} + 1{\cdot}63\ H_2O\ (+CO_2) \quad (2)$$

accounts for the replacement of amphibole by clinopyroxene. Reaction (2) is somewhat simplified, as the amphibole breakdown reaction also produces some minor biotite (1·4 wt %), which results from the minor K contained in amphibole.

Both the amphibole to clinopyroxene and the biotite to phengite reactions consume zoisite. Zoisite is most abundant in the low-*T*, low-*P* portion of the *P*–*T* grid, and decreases from 40 wt % at 750°C, 2·0–2·3 GPa to 9 wt % at 850°C, 2·5–3·5 GPa. In a first step, the zoisite abundance is reduced by 10% relative through the amphibole to clinopyroxene reaction, then, across the biotite to phengite reaction, zoisite is reduced to one-fourth of the initial amount, defining a wide *P*–*T* region of stepwise and progressive zoisite dehydration.

The fluid-saturated solidus reactions (850–950°C)

The isobaric sections (Fig. 7b and c) illustrate the melting of mica + quartz/coesite + zoisite + dolomite. With increasing *T*, the first melt fractions at 2·0 and 2·5 GPa constitute 10 and 7 wt %, respectively, at 3·0 GPa 19 wt %, and at 3·5 GPa 24 wt %. At 2·0 and 2·5 GPa, the persistence of mica (9 and 12 wt %), zoisite (22 and 9 wt %) and amphibole (8 wt %; only at 2·0 GPa) indicates a wider *T* range for the multivariant solidus reaction, with a more steadily increasing melt fraction than at 3·0 and 3·5 GPa. In these latter two experiments, no mica and only 2 wt % zoisite (at 3·5 GPa) are left, thus resulting in larger apparent melt fractions just above the solidus. However, melt proportions also reflect the extent of overstepping the solidus in *T*.

*Table 6: Melt compositions**

P(GPa)/*T*(°C):	2·0/850	2·0/950	2·0/1050	2·3/900	2·5/850	2·5/950	2·5/1050	2·5/1100	2·5/1200
No. of analyses:	3	6	25	4	12	11	27	23	28
SiO_2	70·27 (0·34)	70·51 (1·02)	71·09 (1·10)	71·60 (1·19)	72·15 (0·93)	71·58 (0·99)	69·54 (1·02)	70·74 (0·95)	59·70 (0·49)
Al_2O_3	13·12 (1·04)	16·23 (0·52)	16·23 (0·59)	15·44 (1·82)	13·43 (0·28)	15·66 (2·04)	17·03 (0·39)	16·19 (0·19)	21·63 (0·28)
MgO	1·77 (0·71)	1·12 (0·65)	1·31 (0·13)	0·85 (0·26)	0·71 (0·12)	0·78 (0·17)	1·27 (0·23)	1·49 (0·27)	4·08 (0·34)
CaO	5·18 (1·33)	4·31 (1·25)	4·47 (0·33)	3·62 (0·33)	3·40 (0·18)	3·29 (0·27)	5·56 (0·33)	5·39 (0·30)	11·75 (0·20)
K_2O†	9·66 (0·03)	7·83 (0·47)	6·89 (0·44)	8·50 (0·55)	10·32 (0·65)	8·70 (0·29)	6·60 (0·54)	6·19 (0·26)	2·84 (0·07)
Total (wt %)	92·71	92·13	94·44	90·62	90·15	90·68	90·95	94·06	95·60
Si	3·157 (23)	3·116 (21)	3·125 (22)	3·164 (48)	3·219 (13)	3·162 (68)	3·070 (1(9	3·109 (17)	2·681 (19)
Al_{tot}	0·695 (60)	0·846 (20)	0·841 (29)	0·804 (88)	0·706 (9)	0·816 (101)	0·886 (15)	0·839 (10)	1·145 (17)
Mg	0·118 (48)	0·074 (33)	0·086 (9)	0·056 (18)	0·047 (8)	0·051 (11)	0·083 (15)	0·097 (19)	0·273 (23)
Ca	0·249 (64)	0·204 (13)	0·211 (17)	0·171 (18)	0·162 (8)	0·156 (14)	0·263 (16)	0·254 (15)	0·565 (7)
K	0·554 (2)	0·441 (33)	0·386 (25)	0·479 (36)	0·587 (36)	0·490 (18)	0·372 (30)	0·347 (14)	0·163 (3)
Total cations (p.f.u.)	4·773	4·681	4·648	4·674	4·722	4·675	4·673	4·646	4·828
Al/(K + 2Ca) (p.f.u.)	0·66	1·00	1·04	0·98	0·77	1·02	0·99	0·98	0·89
Al/K (p.f.u.)	1·25	1·92	2·18	1·68	1·20	1·66	2·38	2·42	7·03
Qtz	26·8	30·6	34·5	31·0	28·4	30·7	31·7	34·9	22·2
Plag	8·3	21·8	23·1	17·5	6·6	16·7	27·9	27·0	58·4
Kfsp	64·9	47·6	42·4	51·5	65·0	52·6	40·4	38·1	19·4

P(GPa)/*T*(°C):	2·5/1250	2·5/1300	3·0/950	3·5/950	3·5/1150	3·5/1200	3·5/1250	3·5/1300	3·7/1100
No. of analyses:	13	12	7	11	10	12	17	24	11
SiO_2	58·66 (0·27)	55·52 (0·36)	72·60 (0·87)	74·63 (1·34)	68·89 (0·34)	65·36 (0·67)	62·00 (0·36)	59·42 (0·28)	72·42 (1·58)
Al_2O_3	21·43 (0·27)	22·38 (0·22)	13·10 (0·25)	13·38 (0·50)	15·31 (0·11)	17·12 (0·23)	19·08 (0·17)	19·51 (0·20)	15·15 (1·65)
MgO	4·41 (0·12)	7·55 (0·24)	0·49 (0·16)	0·49 (0·12)	1·73 (0·25)	2·47 (0·09)	3·32 (0·07)	4·82 (0·17)	0·59 (0·22)
CaO	12·76 (0·13)	12·46 (0·10)	2·58 (0·32)	2·45 (0·20)	7·98 (0·13)	10·82 (0·20)	12·14 (0·13)	13·31 (0·10)	3·95 (0·75)
K_2O†	2·75 (0·04)	2·09 (0·03)	11·22 (0·82)	9·05 (1·12)	6·09 (0·09)	4·23 (0·05)	3·45 (0·05)	2·95 (0·04)	7·88 (0·97)
Total (wt %)	91·91	92·96	91·98	90·08	89·00	89·88	90·14	91·06	92·53
Si	2·648 (7)	2·516 (8)	3·244 (24)	3·280 (27)	3·064 (12)	2·922 (14)	2·788 (7)	2·691 (8)	3·187 (63)
Al_{tot}	1·140 (11)	1·195 (9)	0·690 (8)	0·693 (23)	0·803 (6)	0·902 (13)	1·012 (9)	1·041 (9)	0·786 (78)
Mg	0·296 (7)	0·510 (14)	0·033 (11)	0·032 (8)	0·115 (16)	0·165 (6)	0·222 (5)	0·325 (11)	0·039 (15)
Ca	0·617 (6)	0·605 (5)	0·124 (16)	0·115 (9)	0·380 (6)	0·518 (11)	0·585 (6)	0·646 (5)	0·186 (38)
K	0·158 (2)	0·121 (2)	0·639 (48)	0·507 (62)	0·345 (5)	0·241 (3)	0·198 (3)	0·170 (2)	0·442 (54)
Total cations (p.f.u.)	4·861	4·947	4·730	4·627	4·707	4·748	4·805	4·874	4·641
Al/(K + 2Ca) (p.f.u.)	0·82	0·90	0·78	0·94	0·73	0·71	0·74	0·71	0·97
Al/K (p.f.u.)	7·20	9·91	1·08	1·37	2·32	3·74	5·10	6·12	1·78
Qtz	20·4	14·1	27·1	35·3	32·9	30·9	25·9	21·6	34·0
Plag	60·2	70·1	2·8	10·0	26·7	39·9	49·8	56·3	18·5
Kfsp	19·4	15·8	70·2	54·7	40·4	29·2	24·3	22·1	47·6

*Based on eight oxygens. Values in parentheses are 1 SD in terms of last digit(s).
†K_2O content adjusted for K loss. Calculated from mass-balanced fractions and bulk K_2O.

The fluid-present solidus at ≥2·5 GPa is constrained to a narrow reaction band (≤50°C), determined by the almost immediate breakdown of phengite, occurring close to 850°C at 2·5 GPa (Fig. 3d), at 900°C at 3·0 GPa, and at <950°C at 3·5 GPa (Fig. 3b). Incongruent melting of phengite + coesite + zoisite + fluid resulting in melt + clinopyroxene + kyanite occurs through the reaction

$$1{\cdot}00\ \text{phe} + 0{\cdot}36\ \text{zo} + 2{\cdot}62\ \text{qz/cs}\ (+\text{fluid} + \text{dol}) = 1{\cdot}53\ \text{melt} + 0{\cdot}56\ \text{cpx} + 1{\cdot}03\ \text{ky} \quad (3)$$

Table 7: Dolomite, zoisite and garnet compositions

Run no.	dolomite X_{Mg}molar	zoisite Mg (p.f.u.)	garnet X_{gros}
MC-05c	0·480	0·087 (42)	–
MC-04c	–	0·084 (72)	–
MC-08	–	–	–
MC-15	–	–	0·220
MC-11	0·483	0·082 (24)	–
MC-20	0·466	0·118 (12)	–
MC-12	–	0·125 (43)	–
MC-13	–	–	–
MC-22	0·472	0·135 (40)	–
MC-17	0·488	0·096 (14)	–
MC-21	0·474	–	–
MC-06c	0·477	0·137 (63)	–
MC-24	0·474	0·066 (14)	–
MC-03c	0·475	0·068	–
MC-38c	–	–	–
MC-07	–	–	–
MC-09	–	–	0·253
MC-26	–	–	0·241
MC-27	–	–	0·241
MC-31	–	–	0·282
MC-35	–	–	–
MC-16	0·479	0·081 (41)	–
MC-25	0·475	0·081 (8)	–
MC-01	0·489	0·071 (16)	–
MC-36	0·459	0·050	–
MC-18	0·469	–	–
MC-02	0·467	0·073 (32)	–
MC-23	–	0·013 (23)	–
MC-28	–	–	0·335
MC-29	–	–	0·381
MC-30	–	–	0·353
MC-34	–	–	0·292
MC-37	–	–	0·341

$X_{Mg} = Mg/(Ca + Mg)$. Values in parentheses are 1 SD in terms of last digit(s).

at 3·0 and 3·5 GPa. This reaction also consumes dolomite, which is not mass balanced as neither the CO_2 content of the fluid nor that of the melt are known. Because of the much larger solubility of H_2O than of CO_2 in siliceous melts (e.g. Holloway & Blank, 1994; Dixon *et al.*, 1997; Wallace & Anderson, 1999; Papale, 1999), it is expected that fluid compositions shift to higher X_{CO2} at the solidus.

Below 2·5 GPa, initial melting occurs through incongruent melting involving biotite (and amphibole) instead of phengite. At 2·4 GPa and 860°C the breakdown of biotite and dolomite coincide. The solidus at 2·4 GPa also corresponds to biotite-out, whereas zoisite and quartz melt out 50°C higher. At 2·3 GPa and below, dolomite breaks down at subsolidus conditions. No other carbonate is formed; thus, the CO_2 previously contained in dolomite enters the fluid. When dolomite breaks down the X_{CO2} of the fluid phase is expected to increase, reducing the T stability of the hydrous phases and increasing solidus temperatures.

Similar to solidus reaction (3), the calculated melting reaction at 2·3 GPa consumes biotite + quartz + zoisite + fluid to produce melt + clinopyroxene + kyanite through the reaction

$$1{\cdot}00\ \text{bt} + 1{\cdot}15\ \text{zo} + 5{\cdot}21\ \text{qz}\ (+\text{fluid} \pm \text{dol}) = 1{\cdot}88\ \text{melt} + 2{\cdot}15\ \text{cpx} + 1{\cdot}57\ \text{ky}. \quad (4)$$

Compared with the phengite-controlled solidus reaction (3), larger proportions of zoisite (35 wt %) and quartz (18 wt %) are consumed for the massive production of clinopyroxene (maximum 48 wt %) and kyanite (19 wt %) across reaction (4).

Below 2·0 GPa the peritectic solidus reaction (at 840°C) produces amphibole instead of clinopyroxene. Dolomite is not involved in this reaction, as the upper T stability of dolomite + quartz is overstepped at these relatively low pressures. Mass balance of the phases in the experiment at 850°C, 2·0 GPa yields the melting reaction

$$1{\cdot}00\ \text{bt} + 0{\cdot}63\ \text{zo} + 4{\cdot}05\ \text{qtz}\ (+\text{fluid}) = 1{\cdot}44\ \text{melt} + 0{\cdot}52\ \text{amph} + 0{\cdot}71\ \text{ky} \quad (5)$$

which should be the fluid-saturated solidus reaction below 2 GPa.

Melting above 950°C

After the disappearance of mica, quartz/coesite, and zoisite, melt proportions increase only slightly between 950 and 1050°C through congruent melting of clinopyroxene. Towards higher temperatures, melt proportions increase substantially when incongruent melting of clinopyroxene + kyanite forms garnet (Fig. 7b and c). This reaction is calculated from the modal abundance changes between 1050 and 1200°C at 2·5 GPa and between 1100 and 1200°C at 3·5 GPa and is typically

$$1{\cdot}62\ \text{cpx} + 0{\cdot}55\ \text{ky} = 1{\cdot}00\ \text{melt} + 1{\cdot}13\ \text{gt}. \quad (6)$$

At 2·5 GPa, this reaction exhausts kyanite forming ≤2 wt % of corundum, whereas at 3·5 GPa clinopyroxene is exhausted before kyanite. At 3·5 GPa, corundum was not observed; nevertheless, the T stability of kyanite and the liquidus were not reached. Both at 2·5 and 3·5 GPa, clinopyroxene disappears between 1200 and 1250°C at 2·5 GPa through the incongruent reaction

$$1{\cdot}96\ \text{cpx} = 1{\cdot}00\ \text{melt} + 1{\cdot}29\ \text{gt}. \quad (7)$$

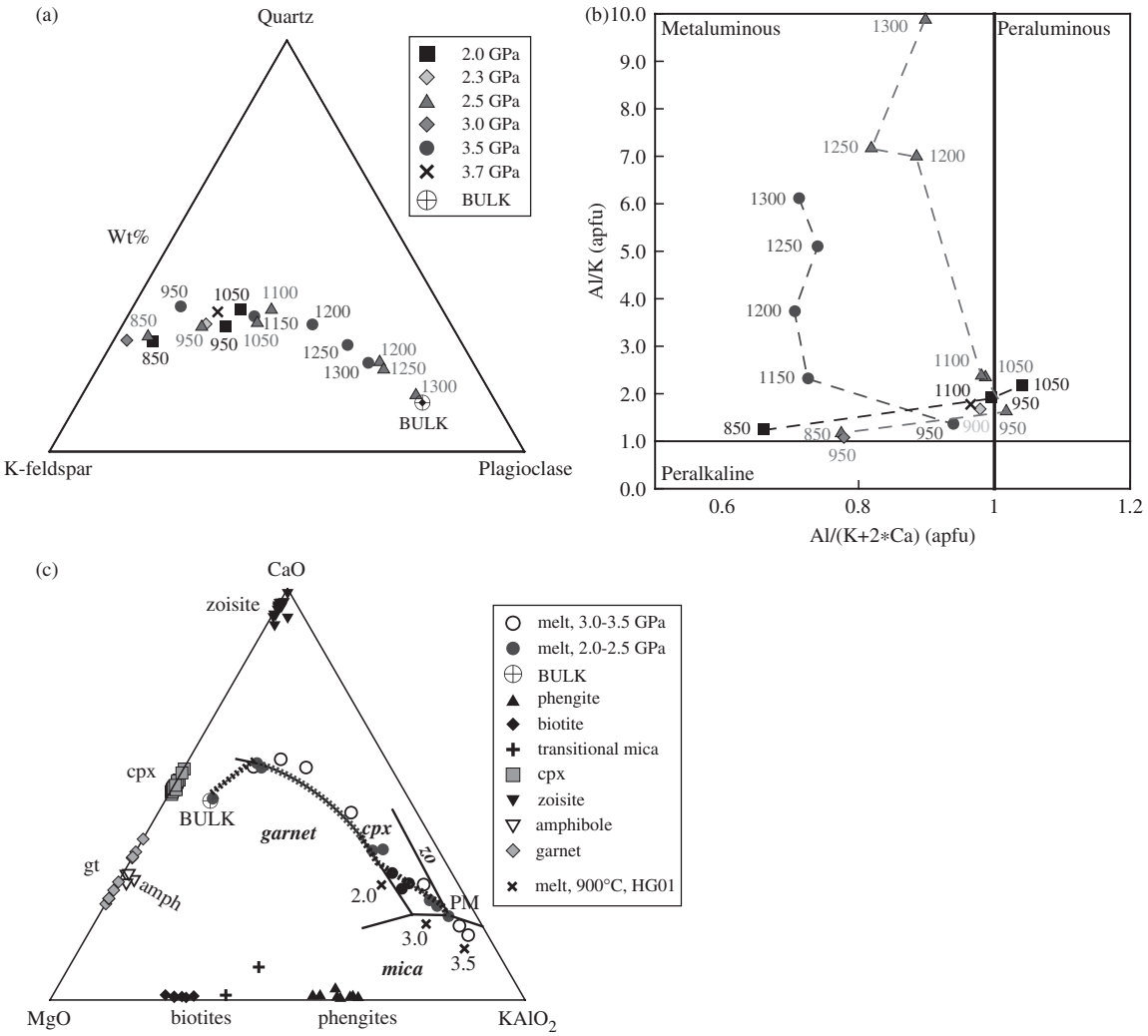

Fig. 6. Melt compositions. (a) Normative composition in terms of quartz, plagioclase and K-feldspar, showing a trend with temperature from quartz- and K-feldspar-rich (syenitic) granite melts towards higher normative plagioclase contents. (b) Aluminosity vs alkalinity of the experimental melts. The peraluminosity increases to ~100–200°C above the solidus, until garnet crystallizes. (c) Projection from quartz/coesite, kyanite, and fluid into MgO–CaO–$KAlO_2$ with analyzed phase compositions and the cotectic melt surface including peritectic points and curves, outlined for the 2·0–2·5 GPa experiments. The bold dashed line represents the melting path (with increasing temperature) for the 2·0–2·5 GPa experiments. Bold italic labels denote the phase present on the melt surface. The peritectic minimum (PM) shifts towards the $KAlO_2$ corner with increasing pressure. ×, Melt compositions from Hermann & Green (2001) (HG01), which correspond to the mica–clinopyroxene–garnet cotectic; these melts also shift towards the $KAlO_2$ apex with pressure (indicated by labels in GPa).

The T interval from 950 to 1100°C at 3·5 GPa includes the melting-out of zoisite and coesite as well as the garnet-in reaction. However, little reaction progress occurs in this interval, only 0·8 wt % clinopyroxene and 1·8 wt % kyanite are consumed, and 1·7 wt % garnet and 3·2 wt % melt are produced (Fig. 7b). In contrast, between 1100°C and slightly more than 1200°C, the melt fraction increases almost constantly by 2·3 wt % melt per 10°C, reflecting continuous melt generation through the peritectic reaction (6).

The projected melting surface

From the melting relations, the topology of a melting surface can be deduced for the KCMASH–CO_2 system. For this purpose, melt compositions are projected from quartz/coesite, kyanite, and fluid, thus leaving a three-component system with the principal components MgO, CaO and K_2O (Fig. 6c).

As expected, the lowest T melt occurs close to the $KAlO_2$ corner, where peritectic melting (PM, Fig. 6c) takes place through the peritectic reaction (3) or (4) producing clinopyroxene. In our bulk composition, phengite melts out first, and melts then evolve along the peritectic curve zoisite = clinopyroxene + melt. Both the peritectic point PM and the peritectic curve shift towards $KAlO_2$ with P, resulting in a clear difference of melt compositions between the experiments at 2·0–2·5 and 3·5 GPa.

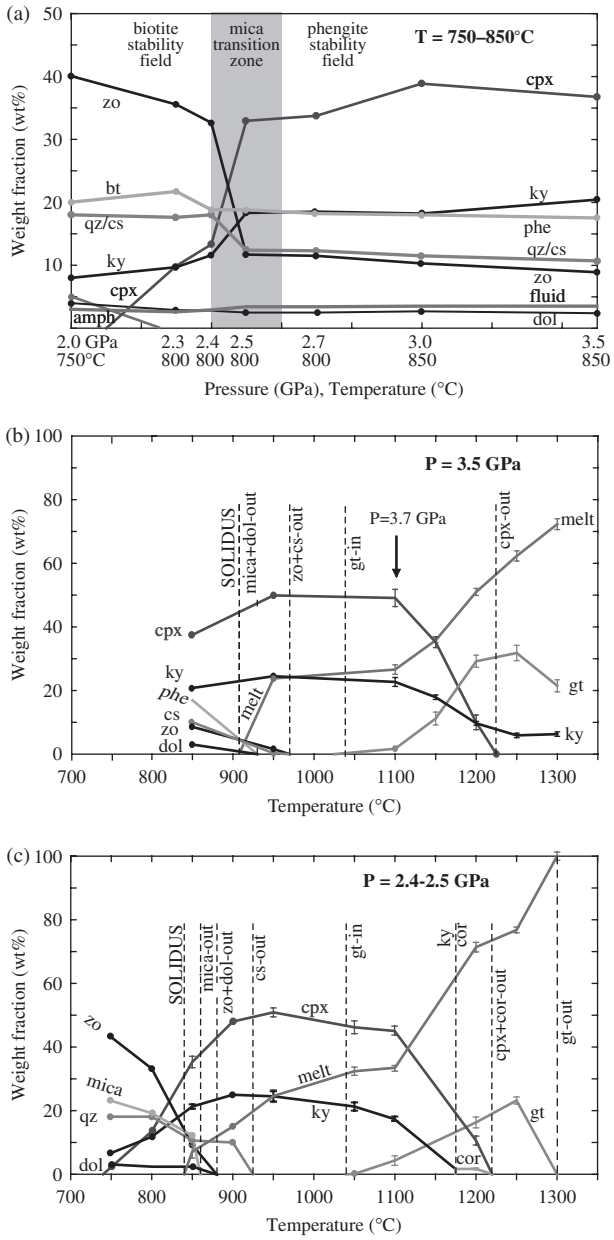

Fig. 7. Calculated phase proportions (in wt %) with pressure for (a) subsolidus temperatures between 750 and 850°C and with temperature for (b) 3·5 GPa, and (c) 2·4–2·5 GPa. The grey field in (a) indicates the pressure range for the biotite to phengite reaction. In (b) and (c) solidus and phase stability limits are shown.

When zoisite is exhausted with further increasing T, melts leave the zoisite/clinopyroxene peritectic curve and evolve on the clinopyroxene surface, simply consuming clinopyroxene. At 1050–1100°C, melts encounter the peritectic curve clinopyroxene = garnet + melt on which they evolve until clinopyroxene is exhausted. It should be noted that both clinopyroxene and garnet vary in their composition along the MgO–CaO edge of the triangle. Clinopyroxene becomes more aluminous through Tschermak's exchange mainly with T, thus moving towards the CaO corner, and garnet becomes calcium-enriched with P (Fig. 5).

COMPARISON WITH PREVIOUS HIGH-PRESSURE EXPERIMENTAL STUDIES

Previous high-P experimental studies of metasediments were mostly performed on CO_2-free pelites and their simplified synthetic subsystems. First, we compare subsolidus phase relations concerning the biotite to phengite reaction and then the various solidi, melting reactions, and melt compositions.

The biotite to phengite reaction and subsolidus phase relations

As expected, the stability of biotite in KCMASH–CO_2 and subsystems is strongly dependent on bulk composition. Somewhat surprisingly, in a kyanite-saturated system bulk X_{Ca} [molar $Ca/(Ca + Mg + Fe^{2+})$] in combination with the Ca-phase(s) coexisting with the potassic micas determine the P stability of biotite.

Quartz + kyanite-saturated bulk compositions more calcic than the tie-line clinopyroxene–phengite, as investigated in this study (Fig. 8a), have biotite reacting completely to phengite within a narrow P field. Bulk compositions in the triangle cpx–phengite–biotite [e.g. P1 of Hermann & Green (2001) and Hermann (2002) (Fig. 8a)] have phengite and biotite coexisting over a larger P interval and to higher pressures. Experiments in KCMASH at 2·0–4·5 GPa, 680–1050°C with 2–5 wt % H_2O (Hermann & Green, 2001; Hermann, 2002) had biotite and phengite coexisting from 2·5 to 3·9 GPa at 780°C (see discussion below). The appearance of phengite above 2·5 GPa in Hermann's experiments is similar to our results; on the other hand, biotite is stable to 1 GPa higher pressures and 50°C higher temperatures (at 2·5 GPa) than in our study. This reflects the lower $Ca/(Ca + Mg)$ of 0·35 of Hermann's bulk composition, compared with our experiments with a bulk X_{Ca} of 0·54; the lower X_{Ca} stabilizes biotite and results in orthopyroxene forming from biotite through the H_2O-conservative reaction

$$1 \cdot 00\ \text{phl} + 0 \cdot 63\ \text{ky} + 2 \cdot 37\text{qz/cs} = 1\ \text{cel}_{50} + 1 \cdot 32\ \text{opx} \quad (8)$$

balanced for phengite with the composition cel_{50} and for orthopyroxene with 0·2 Al p.f.u. In both studies, amphibole is stable only below 2·2 GPa at 800°C to <3·0 GPa at 750°C, replacing clinopyroxene with decreasing P (Hermann, 2002).

In both studies, garnet occurs at temperatures and pressures higher than the biotite to phengite reaction. This is in contrast to Mg + Fe-rich synthetic and to most natural

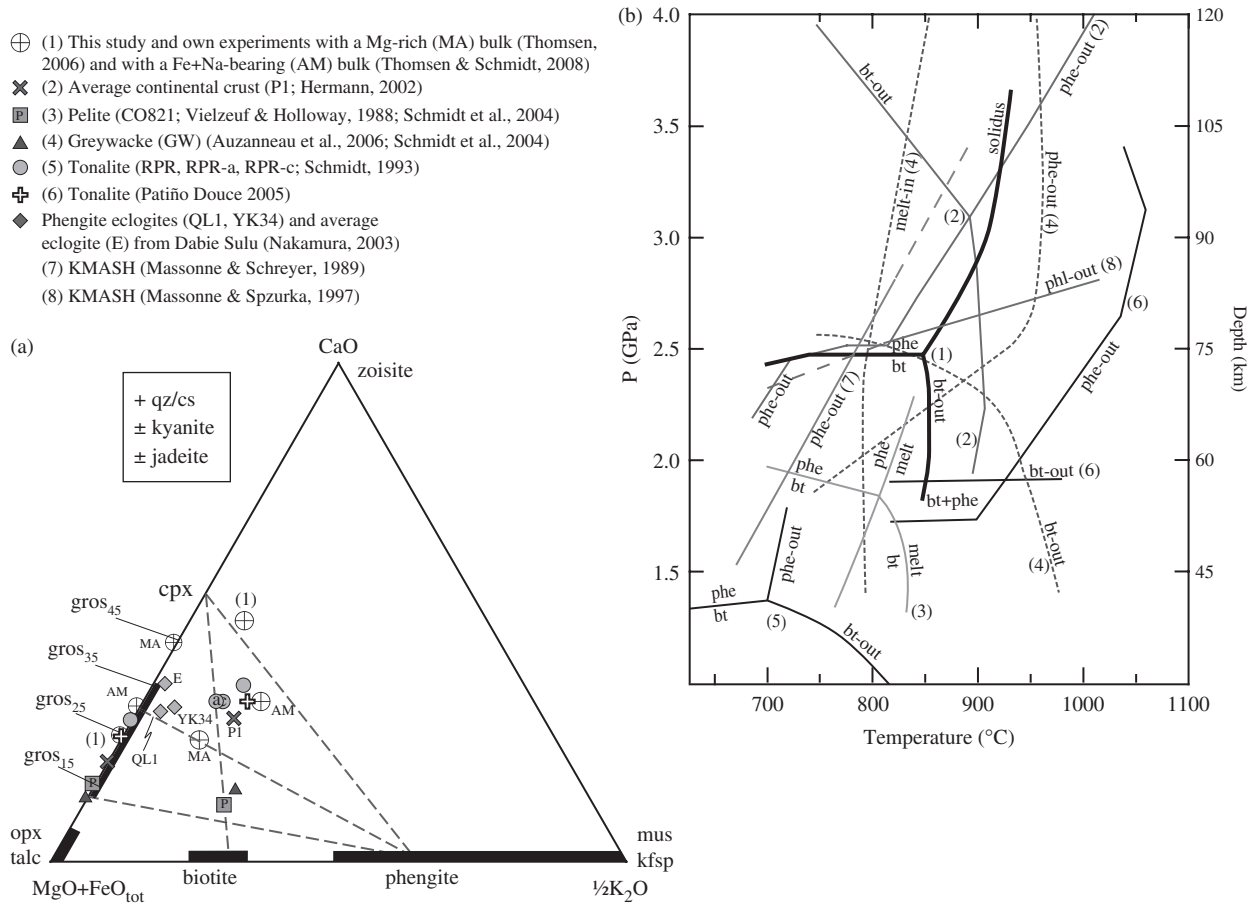

Fig. 8. Comparison of bulk compositions relevant for the biotite to phengite reaction from different studies in (a) CaO–(MgO + FeO_{tot})–½K_2O, projected from quartz/coesite, kyanite, and albite/jadeite, and (b) experimentally determined stability fields of biotite and phengite and loci of solidi in a *P*–*T* diagram. (1) This study, based on the experimental results and chemographic analyses of phase relations from Figs 1 and 2. (2) Biotite and phengite stability in KCMASH for average continental crust (Hermann & Green, 2001; Hermann, 2002). (3) Biotite to phengite reaction and mica-controlled melting in KFMASH pelites (Vielzeuf & Holloway, 1988). (4) Biotite and phengite-out and solidus in greywacke (Auzanneau *et al.*, 2006). (5) Biotite to phengite reaction and their melting reactions in fluid-saturated tonalite (Schmidt, 1993). (6) Biotite and phengite stability in fluid-absent tonalite (Patiño Douce, 2005). (7) Phengite-out in KMASH (Massonne & Schreyer, 1989). (8) Phlogopite-out in KMASH (Massonne & Spzurka, 1997). The left side of the diagram in (a) is labelled with garnet composition and the experimental garnet compositions are denoted with symbols corresponding to those used for the appropriate bulk composition.

compositions, for which the formation of garnet and stabilization of the garnet–phengite tie-line delimits the *P* stability of biotite.

The strongly magnesian composition MA (Fig. 8a), which with 15·22 wt % MgO and a molar Ca/(Ca + Mg) of 0·28 is situated on the Mg-rich side of the clinopyroxene–biotite tie-line, preserves biotite to high pressures without forming phengite (Thomsen, 2006). These experiments at 2·5–6 GPa, 850–1100°C yielded biotites with octahedral occupancies of 2·44–2·91 a.p.f.u. stable to 6 GPa, and a garnet with up to 48 mol % grossular, but no phengite, as the biotite–garnet tie-line encompasses the bulk composition. However, direct comparison with the above studies is difficult, as the composition MA is not quartz/coesite-saturated, and did not yield orthopyroxene.

In the KMASH experiments of Massonne & Schreyer (1989) the reaction

$$\text{tc} + \text{phe} = \text{bt} + \text{ky} + \text{qz} + \text{fluid} \qquad (9)$$

defines the lower-*P* occurrence of phengite at 1 GPa, 610°C to 2·7°C, 800°C, crossing our mica reaction at 2·5 GPa, 770°C (Fig. 8b, label 7). This reaction also occurs in the study by Herman (2002), but exhausts talc and does not delimit the stability of phengite in the P1 bulk composition, corresponding to a simplified continental crust average.

The upper *P* stability limit of phlogopite + kyanite + quartz in KMASH is defined through the reaction

$$\text{phl} + \text{ky} + \text{qz} = \text{phe} + \text{pyrope} \qquad (10)$$

estimated to be located at 2·5 GPa, 810°C to 2·7 GPa, 1000°C (Massonne & Szpurka, 1997; Fig. 8b, label 8).

In reaction (10), talc is replaced by pyrope; the reaction thus becomes fluid absent and would not terminate at the fluid-saturated solidus. The crucial role of Fe in such a garnet-forming reaction is illustrated by the location of the Fe-equivalent of reaction (10) at <1·0 GPa (Massone & Szpurka, 1997).

Finally, Hoschek (1990) has determined that the reaction

$$\text{phe} + \text{tc} + \text{trem} = \text{bt} + \text{zo} + \text{qz} + \text{fluid} \qquad (11)$$

in KCMASH is located from 1·7 GPa, 700°C to 2 GPa, 740°C. This reaction was determined for a bulk X_{Ca} of 0·29, is the equivalent to reaction (1) for aluminosilicate-undersaturated bulk compositions, and is located at somewhat lower pressures in the amphibole stability field.

Natural (CO_2-free) pelite and greywacke are composed of biotite + plagioclase + quartz ± kyanite at low pressures. This assemblage reacts to phengite + garnet + clinopyroxene + quartz ± kyanite with increasing P through reaction (10) when kyanite is present, and through the reaction

$$\text{bt} + \text{plag} + \text{gt} = \text{phe} + \text{cpx} + \text{qz} \qquad (12)$$

in aluminosilicate-undersaturated compositions. For a natural pelite, Vielzeuf & Holloway (1988) determined the biotite to phengite reaction (11) to be located at 1·8–2·0 GPa at 700–800°C (Fig. 8, label 3). In a natural greywacke, Auzanneau (2005) and Auzanneau *et al.* (2006) determined reaction (13) to be located at 800°C between 1·8 and 2·6 GPa, narrowing at 900°C to 2·2 GPa (Fig. 8, label 4). Both bulk compositions have a low X_{Ca} (0·15 and 0·19, respectively), and result in a grossular-poor garnet, such that the tie-line phengite–garnet is less calcic than the bulk composition, effectively terminating the stability of biotite to higher pressures (Fig. 8a).

Tonalites contain, similar to greywackes, K_2O and CaO as major components, and have X_{Ca} typically around 0·4, which is higher than for carbonate-free metasediments, but comparable with carbonated pelites. In tonalites, the biotite to phengite reaction takes place at relatively low pressures. For the H_2O-saturated experiments of Schmidt (1993) (Fig. 8, label 5) this reaction occurs over a sharp reaction field at 1·3–1·4 GPa at 650°C, through

$$\text{phe} + \text{amph} = \text{bt} + \text{plag} + \text{kfsp} + \text{qz} + \text{fluid}. \qquad (13)$$

This reaction involves both feldspars and amphibole, and biotite or phengite coexist with amphibole + plagioclase + epidote + quartz. For the H_2O-undersaturated, more aluminous tonalite of Patinõ Douce (2005) (Fig. 8, label 6) the P stability of biotite has been defined from topological constrains resulting from the experiments. This tonalite saturates in kyanite at the biotite to phengite reaction. Apparently, this simplifies the biotite–phengite equilibrium, and in this natural system an Fe-bearing equivalent of reaction (11) occurs around 1·9 GPa (800–900°C) where biotite or phengite coexists with kfsp + cpx + garnet + quartz + kyanite.

The upper P stability limit of amphibole in our experiments is similar to that determined for mafic compositions, extending to no more than 2·5 GPa at 700°C [summarized by Poli & Schmidt (2002)]. In our aluminous system, reaction (2) results in kyanite, whereas the amphibole breakdown in basaltic systems generates less aluminous phases such as chloritoid (Poli & Schmidt, 1995; Forneris & Holloway, 2003). Zoisite + cpx + garnet + coesite is generally limited to below 3 GPa in natural bulk compositions (Poli & Schmidt, 2002). The higher P stability limit of zoisite in our experiments thus reflects the Fe-free character and the high X_{Ca} ratio of our bulk composition compared with most other bulk compositions studied. Similarly, the absence of Fe shifts the occurrence of garnet to higher pressures, garnet being a product in the reaction delimiting the zoisite P stability.

In summary, two compositional parameters exert a bulk control on the biotite P stability: the X_{Ca} and the aluminosity of the system. For natural carbonate-bearing metapelites, the amount of sedimentary calcite or dolomite will determine the bulk Ca/(Ca + Mg + Fe), aluminosilicate saturation being generally achieved. Most subsolidus reactions are affected to a small extent only by the presence of CO_2, as X_{CO2} in a fluid at >2 GPa is low at subsolidus conditions (Kerrick & Connolly, 2001; Connolly, 2005). The biotite to phengite reaction in synthetic Fe-free systems has a limited application to natural bulk compositions because the formation of pyrope–grossular solid solution is retarded to pressures above the biotite to phengite reaction with respect to natural Fe-rich systems. This may then lead to the stabilization of orthopyroxene (Hermann, 2002), which is generally not observed in metasedimentary or continental crust bulk compositions as considered here. Iron partitions strongly into garnet, increasing the garnet stability field in natural compositions to much lower temperatures and pressures. As discussed above, the shift of the garnet appearance to higher pressures in Fe-free synthetic systems also stabilizes zoisite, which decomposes to grossular + kyanite + coesite + H_2O at pressures as high as 7 GPa (in CASH, Poli & Schmidt, 1998).

The fluid-saturated KCMASH system with and without CO_2

The experiments of this study and those of Hermann & Green (2001) and Hermann (2002) define key reactions in subducted crustal lithologies saturated in quartz/coesite + kyanite + fluid; those of the present study include carbonates and CO_2, the others do not. Schreinemaker's analysis of the two systems (Fig. 9) revealed that reactions and reaction conditions are similar for amphibole and phengite, but not for biotite, garnet and orthopyroxene; orthopyroxene occurs only in the CO_2-absent system (Fig. 9b).

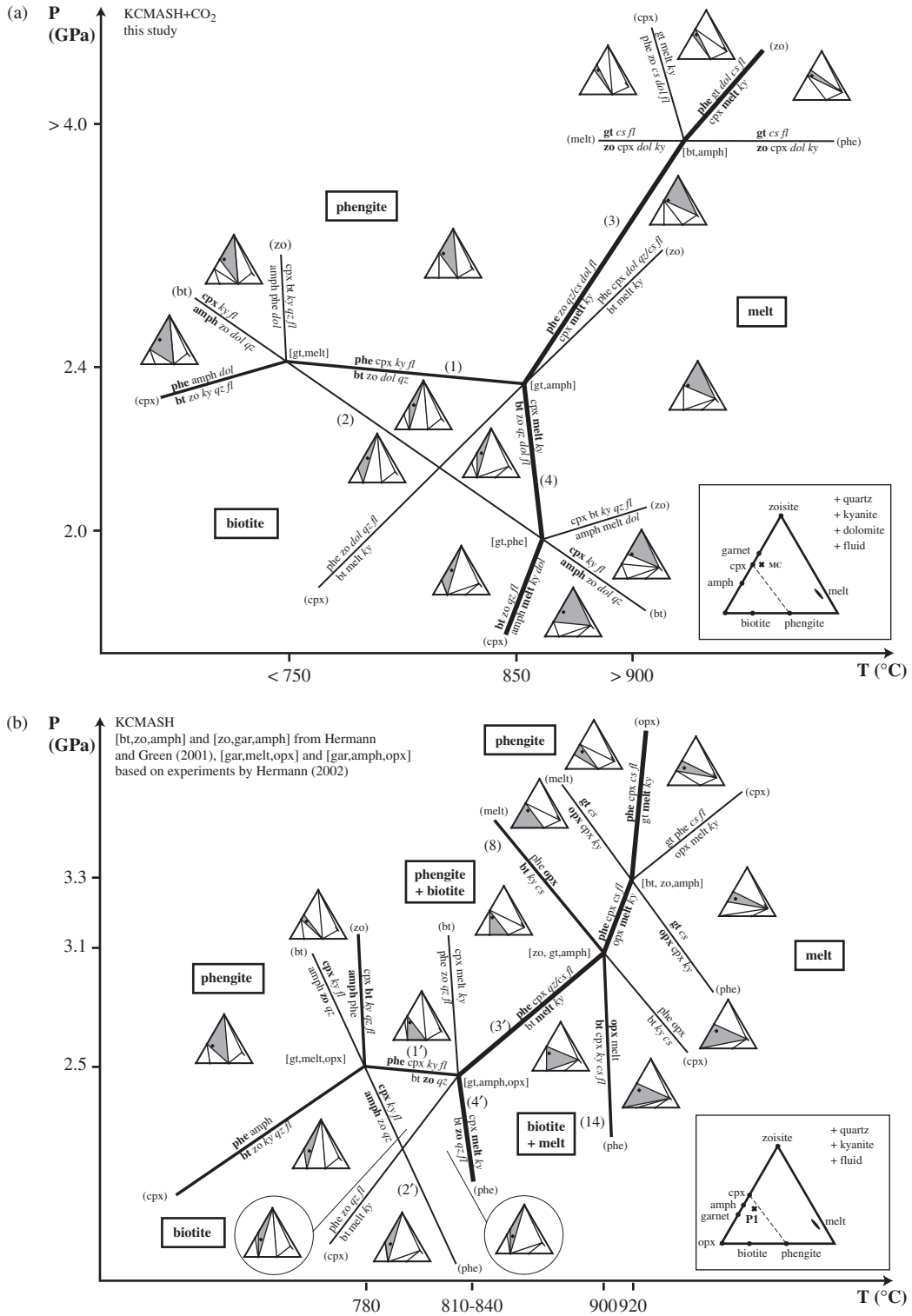

Fig. 9. Grids of reactions as determined for (a) the KCMASH + CO_2 system of this study and (b) the KCMASH system of Hermann & Green (2001) and Hermann (2002). The reactions are derived from Schreinemaker analysis and located through the experiments, except for the reactions around the invariant point [bt,amph], which are located through thermodynamic calculations. Reactions that have the projecting phases absent are not shown, and phases exhausted when crossing a reaction are labelled in bold. Bold lines denote the solidus of the reaction grid; lines of intermediate thickness delimit the stability fields of biotite and phengite; the stability fields of the potassium phases are indicated in boxes. The invariant point [gt,phe] is metastable with respect to the dolomite decomposition reaction dolomite + quartz = diopside + fluid. Numbers in parenthesis correspond to reactions *discussed* in the text. Axes are not to scale and pressures and temperatures indicate the location of the invariant points.

Our experiments (Fig. 2), which are in a true K_2O–CaO–MgO–Al_2O_3–SiO_2–H_2O–CO_2 system, define two invariant points [gar,melt] and [gar,amph] near 2·4 GPa and 750–850°C. A further invariant point [bt,amph], describing garnet-in with P, is added from the pseudosection calculations.

The experiments of Hermann & Green (2001) and Hermann (2002) are in a K_2O–CaO–MgO–Al_2O_3–SiO_2–H_2O system with 0·2 wt % Na_2O and with 1400 ppm rare earth elements (REE) + Y added. As discussed below, the addition of REE strongly influences the stabilities of zoisite and probably garnet. To interpret the phase relations of these experiments, two invariant points defining the stabilities of orthopyroxene and garnet ([bt,zo,amph] and [zo,gar,amph], Fig. 9 b) were taken from Hermann & Green (2001, fig. 7, left). The invariant points [gar,melt,opx] and [gar,amph,opx] near 2·5 GPa and 780–840°C (Fig. 9b), equivalent to [gar,melt] and [gar,amph] in the CO_2-present system (Fig. 9a), are redefined through a Schreinemaker analysis of the original experiments.

The resulting reaction grid (Fig. 9b) differs substantially from the analysis by Hermann (2002, fig. 9); the latter unfortunately contains five stoichiometrically incorrect reactions and consequently Schreinemaker errors. Two further problems in the study by Hermann (2002) are that (1) neither in the experiments, nor in the definition of the reactions of Hermann (2002, fig. 9) are fluid and melt clearly defined, and (2) several important reactions depicted as univariant are not univariant in the experiments, as phases that could coexist only along a univariant reaction in Hermann's petrogenetic grid (e.g. garnet + orthopyroxene) coexist over a much wider P and/or T range. Problem (2) was recognized by Hermann (2002) for zoisite, which concentrates light REE stabilizing allanite-rich zoisite. Similarly, one possible reason for the coexistence of garnet + orthopyroxene over a wide T interval (≥100°C at 2 and 3 GPa), is that a small fraction of garnet formed at the garnet-in reaction could be stabilized by concentrating heavy REE + Y. The effect of problem (1) can be best understood formulating two extreme hypotheses: first, all experiments are fluid-saturated and all of the reactions involving melt should also involve fluid [as in Fig. 9b and fig. 7 (left) of Hermann & Green (2001)]. However, in this case the grid of Hermann (2002) would only allow for melting ~100°C above the experimental temperatures at which glass has been observed. The second hypothesis is that experiments involving melt were not fluid-saturated, in which case the projection from fluid becomes invalid, and all univariant reactions in Hermann (2002, fig. 9) containing melt would describe fluid-absent melting and become divariant fields. However, as the experiments of Hermann (2002) were, at least, fluid-saturated at subsolidus conditions, this second hypothesis leads to a lack of fluid-saturated melting reactions in the grid of Hermann (2002). Melting could possibly occur through the reactions, limiting the T stability of talc and amphibole between 700 and 800°C (Hermann, 2002, fig. 9); however, this is implausible as most of these reactions do not involve K_2O or CaO, but any resulting melt would contain all chemical components. Another possible solution is that the melt-in reactions in Hermann (2002) are fluid-saturated but not univariant; instead they constitute ~100°C wide divariant fields whose upper T limit is located by the melt-in reactions of Hermann (2002), the divariance resulting from the 0·2 wt % Na_2O in Hermann's bulk composition and from the REE + Y stabilizing garnet and zoisite. The latter explanation is supported by the presence of 7–9 phases (not accounting for the possible coexistence of fluid with melt) in almost all experiments between 800 and 950–1000°C, whereas a six-component system should allow for only six phases in a divariant field. A larger number of system components probably describes best the experimental results and could solve some of the inconsistencies of the petrogenetic grid, but would not lead to a correct solution for the invariant points also considered by this study.

Our reanalysis of the KCMASH experiments of Hermann (2002) leads to the grid of Fig. 9b, which can be directly compared with the KCMASH + CO_2 grid defined by the experiments of the present study (Fig. 9a). The difference in the projected bulk composition, ours being on the Ca-rich side of the cpx–phengite tie-line and Hermann & Green's being slightly more Mg-rich than the tie-line, has no influence on the general phase and reaction topology at <3·0 GPa and <880°C. The addition of CO_2 shifts subsolidus reactions by 20–30°C [(1, 2) and (1′, 2′)]. As expected, this shift extends the stability of the assemblages on the fluid-bearing side of each reaction. These relatively small shifts can be taken as further evidence of a fluid low in CO_2. Within experimental error, the melting reactions (3, 3′) and (4, 4′) around the equivalent invariant points [gar,amph] and [gar,amph,opx] (near 2·5 GPa in Fig. 9a and b) are located at the same T. Nevertheless, the melt-in reactions in the grid of Fig. 9b do not necessarily define the onset of melting for Hermann's experiments, which occurs at lower temperatures.

The different bulk compositions of the two sets of experiments cause phengite and melt to be consumed through equivalent reactions in both grids; however, this is not the case for biotite. In our bulk composition, only phengite or biotite or melt are stable in a divariant field, whereas for the bulk composition of Hermann & Green (2001), biotite coexists with either phengite or melt over a wide P–T range (Fig. 9b). The subsolidus reaction (1) of biotite to phengite is, apart from the involvement of dolomite in our system, identical in both studies, but is located at 0·1 GPa lower P in our system, again extending the stability of the

assemblage at the fluid-bearing side of the reaction. In our bulk composition, reaction (1) leads to the exhaustion of biotite, whereas in the bulk composition of Hermann & Green, zoisite is exhausted. Similarly, the solidus reaction (4) consumes biotite in our bulk composition, but the equivalent reaction (4') exhausts zoisite in Hermann & Green's bulk composition. This leads to a relatively limited stability field of zoisite (Fig. 9b) and to the persistence of biotite to much higher pressures and temperatures in the Hermann & Green bulk composition. A consequence of the latter is the formation of first orthopyroxene from biotite [reactions (8) and (13)] and then garnet instead of orthopyroxene with increasing P and T (reaction (melt,phe) at the invariant point [bt,zo,amph] in Fig. 9b). For our bulk composition, thermodynamic calculations predict that garnet forms with increasing P from zoisite (reaction (melt,phe) at invariant point [bt,amph] in Fig. 9a). Whereas garnet in the study by Hermann & Green (2002) has a Ca:Mg ratio lower than clinopyroxene, the garnet formed from zoisite in our bulk composition must have a Ca:Mg greater than cpx. Garnet with grossular fractions of 0·24–0·38 only forms in our bulk composition with increasing T through a high-variance reaction at melt fractions >27% when micas, zoisite, carbonate, and quartz/coesite are exhausted.

A further difference between the two sets of experiments concerns the amphibole stability with P. The CO_2-free equivalent of reaction (2), limiting amphibole occurrence in our bulk composition, also occurs in the system of Hermann & Green, but exhausts amphibole only below 2·5 GPa; at higher pressures zoisite is exhausted and therefore, amphibole remains stable.

In summary, the addition of CO_2 to the KCMASH system leads only to small changes in the grid at subsolidus and near-solidus conditions; namely, minor involvement of dolomite in most reactions and a small shift (0·1–0·2 GPa or 20–30°C) of these reactions. The different stability fields for biotite, orthopyroxene, garnet and zoisite for the two bulk compositions are the result of a small but critical shift of the bulk compositions across the clinopyroxene–phengite tie-line. Applied to natural compositions, the main effect of adding calcite to a metasediment may thus not be the effect of the added CO_2 on the phase relations, but the increase in the bulk Ca:(Mg + Fe) ratio.

Comparison of solidus, melting relations and melt compositions

In our system, a melt (which is quenchable) is identified at temperatures about 50–70°C higher than that in the KCMASH experiments of Hermann (2002) (Fig. 8, label 2). Hermann (2002) did not define a solidus, but a melt present region to be distinguished from a region where a non-quenchable liquid is encountered. The low-T melts reported by Hermann & Green (2001) at 900°C have clinopyroxene and garnet ± orthopyroxene coexisting. Their compositions projected from quartz/coesite + kyanite fall close to the garnet–clinopyroxene–mica peritectic (see Fig. 6c); that is, to significantly higher relative Mg contents than the melts of the present study, which locate the zoisite–clinopyroxene–mica peritectic. In fact, the melts of Hermann & Green (2001) are not generated through reaction (3), (4) or (5) involving zoisite, but through reactions involving garnet and/or orthopyroxene instead of zoisite. The T difference for melting may in part be attributed to a minor effect of CO_2, lowering a_{H2O} in the fluid of our study. However, as discussed above, the near-solidus phase relations of Hermann (2002) need to involve the additional 0·2 wt % Na_2O and the REE + Y in their bulk composition. It is thus difficult to attribute the T difference for melting in the two systems to a particular cause. Hermann & Green's (2001) initial melts have slightly peraluminous granitic compositions, and these melts increase in normative K-feldspar with T, whereas our experiments produce metaluminous granitic melts, increasing in normative anorthite content with T (Fig. 6). This reflects the immediate melting-out of micas at the solidus and the lower bulk SiO_2 and higher CaO content in our bulk composition, compared with Hermann & Green (2001).

K-bearing natural eclogites composed of phengite + clinopyroxene + garnet + quartz/coesite ± kyanite form potassic Si-rich granitic melts, comparable with our melts, through phengite + quartz controlled melting at 4 GPa and 850–900°C (Schmidt *et al.* 2004). Below 3·0 GPa, melts are granodioritic, tonalitic or trondhjemitic in composition (Poli & Schmidt, 2002), and at 2·0 GPa, the fluid-absent breakdown of phengite in pelites at 825°C results in granitic melts (Fig. 8, label 3; Vielzeuf & Holloway, 1988). For tonalites, melting above 2·5 GPa is controlled by phengite + quartz/coesite (± zoisite) (Schmidt, 1993; Patiño Douce, 2005). In H_2O-undersaturated tonalite, phengite breaks down at temperatures 150°C higher (Patiño Douce, 2005), compared with our bulk composition, whereas in an H_2O-saturated tonalite bulk composition, the solidus occurs at 600–700°C (Schmidt, 1993). For H_2O-saturated bulk compositions, K-feldspar is generally absent above the solidus (Hermann, 2002; Poli & Schmidt, 2002; this study). If such compositions are also Ca-rich, epidote/zoisite stabilizes instead of plagioclase, resulting in a melting reaction similar to our reaction (5).

A CONFRONTATION OF THE EXPERIMENTAL RESULTS WITH A CALCULATED PSEUDOSECTION

Figure 10 displays a pseudosection calculated for the MC composition of this study, employing the program Perplex (Connolly 1990, 2005) and the database of Holland & Powell (2002) with their appropriate solution

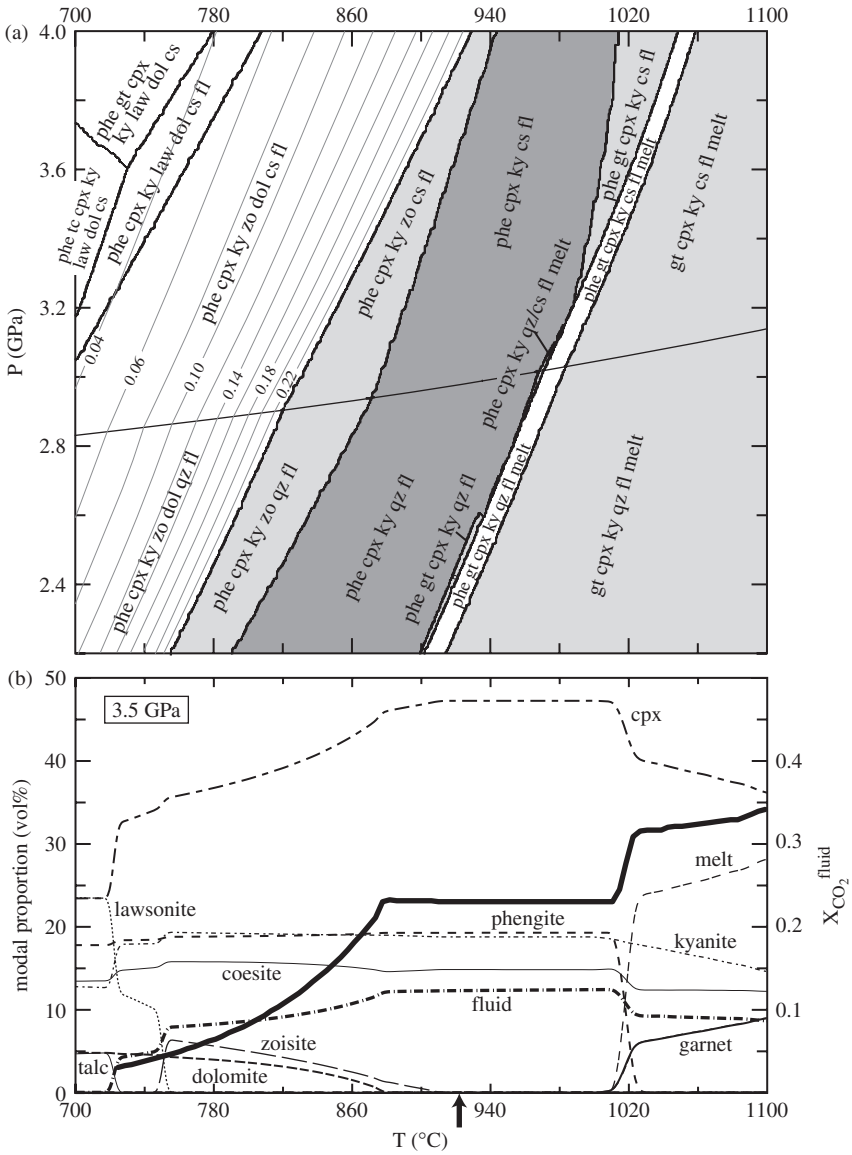

Fig. 10. (a) Pseudosection for the seven-component bulk composition MC of this study, calculated employing Perplex (Connolly, 2005). White fields are divariant; intermediate grey fields three-variant; dark grey fields four-variant. Fluid composition is contoured in terms of X_{CO2} in the fluid-saturated fields at subsolidus conditions. It should be noted that the melt model does not allow for dissolution of CO_2 and thus cannot reproduce the solidus (compare with Fig. 2). (b) Calculated modal proportions in volume per cent at 3·5 GPa. Melt and solids sum to 100%; nevertheless, the abundance of fluid is indicated. The bold continuous line gives the calculated X_{CO2} in the fluid, which is too high when coexisting with melt. It should be noted that the bulk composition is undersaturated in fluid in the high-pressure–high-temperature region of (a), and that fluid composition is fully buffered in the divariant fields. The arrow in (b) indicates the experimentally determined melting temperature at 3·5 GPa.

models for pyrope–grossular, diopside–CaTs, magnesite–dolomite–calcite, muscovite–celadonite, and for a granitic liquid. The model does not allow for CO_2 in the melt and is made such that MgO solubilities in the liquid are negligible. A second shortcoming in the solution models is the lack of a Ca-eskolaite component in clinopyroxene. Nevertheless, the calculated phase relations are similar to the observed experimental results, except for the position of the fluid-saturated solidus, which is 80°C higher in the calculations. Calculated phase proportions (Fig. 10b for 3·5 GPa) correlate reasonably well with the mass-balanced phase proportions of the experiments (Fig. 7b), with the exception of the occurrence and proportion of melt.

The calculations confirm the absence of garnet at fluid-saturated subsolidus and near solidus conditions to >4·0 GPa. Similar to the experiments, garnet-in is a largely *T*-dependent reaction; calculated garnet compositions are $gros_{15}$ at 2·5 GPa and $gros_{22}$ at 3·5 GPa,

underestimating the grossular content by about 10 mol %. Nevertheless, this confirms, that, for a kyanite + quartz/coesite + fluid-saturated Fe-free bulk composition projecting into the clinopyroxene–zoisite–phengite field (Fig. 8), garnet does not form with increasing P at fluid-saturated subsolidus conditions as long as clinopyroxene + zoisite/lawsonite are stable. Garnet of $gros_{57}$ composition (i.e. with a higher Ca:Mg ratio than clinopyroxene) forms in a nearly isobaric reaction at 4·4–4·5 GPa (not shown in Fig. 10) through the breakdown of zoisite + clinopyroxene, which is analogous to the CASH system, in which grossular forms with P upon zoisite breakdown at 6–7 GPa (Poli & Schmidt, 1998, 2004).

A further result of the calculations concerns the proportion and composition of the fluid. At the lowest T–highest P conditions, the stabilization of large proportions of lawsonite leads to fluid undersaturation for the MC bulk composition (<720°C at 3·5 GPa), which in turn results in the stabilization of talc or garnet (Fig. 10a). In the divariant fields where lawsonite + dolomite or zoisite + dolomite coexist with phengite + clinopyroxene + kyanite + quartz/coesite + fluid, the fluid composition is fully buffered, X_{CO2} isopleths lie almost parallel to reaction boundaries, and X_{CO2} increases with T from 0·04 to 0·22 at dolomite-out. As the calculated conditions for dolomite-out are close to the experimentally determined solidus, we assume an X_{CO2} of 0·22 for the fluid composition at the experimental solidus.

Between the dolomite-out and the calculated solidus (three- and four-variant fields at subsolidus conditions in Fig. 10a), fluid compositions are unbuffered and almost constant, corresponding to the bulk volatile composition minus the H_2O bound in phengite; that is, to an X_{CO2} of 0·23, slightly moderated by <2 wt % zoisite present just above dolomite-out. In all melt-present experiments, large bubbles indicate the coexistence of fluid and melt. This would be in agreement with the calculations; however, the absence of a CO_2 component in the melt model forces the melt into fluid saturation (a carbonate phase not being stable in the melt field); thus fluid proportions and compositions in the melt field are not truly modelled by the calculations.

THE EFFECT OF Na IN CARBONATE-SATURATED PELITES

Natural compositions contain significant amounts of Na and Fe; the effect of Fe, mainly on garnet stability, was discussed above. Sodium is incorporated into the jadeitic component in clinopyroxene or into the albite component in plagioclase. The latter leads to stabilization of albite-rich plagioclase to the pressures of the biotite to phengite reaction. However, the participation of albite and jadeite does not cause a major change in the observed phase relations; the observed reactions are only enlarged by an Na component. For the high-P phase relations above the biotite to phengite reaction, Na has a minor effect through lowering the diopside activity in clinopyroxene. The addition of Na (and Fe) would cause lower solidus temperatures as a result of the presence of plagioclase at the solidus below ~2 GPa, and by incorporation of Fe into micas and amphibole. The effect of Na in clinopyroxene on the melting T lessens with P as Na becomes a compatible element and partitions into clinopyroxene at ≥3·0 GPa (Schmidt *et al.*, 2004).

Na is a major component in barroisitic amphiboles, which would be stable in natural compositions to 750°C. Nevertheless, comparison with the experiments of Poli & Schmidt (1995) shows that the effect of Na on the P-dependent amphibole-out is small for sodic–calcic amphiboles; only synthetic purely sodic amphiboles have significantly increased stabilities to 3·2 GPa (Pawley, 1992).

THE CONTRIBUTION FROM CARBONATED PELITES TO THE RECYCLING OF H_2O AND CO_2 AT CONVERGENT MARGINS

For our carbonate-saturated pelite composition, decarbonation and melting reactions could take place only in very high-T subduction zones (Kincaid & Sacks, 1997; Kerrick & Connolly, 2001). Consequently, melting of subducted fluid-saturated carbonate-bearing pelites does not provide a significant volatile source for the generation of arc magmas at most subduction zone conditions. In terms of the global water and carbon cycle, this indicates that the carbonate and K_2O contained in such pelites will be mostly subducted to depths in excess of 120–150 km. Thus, a significant release of the CO_2, K_2O and, partially, H_2O contained in carbonates and hydrates at sub-arc depths would be the exception, carbonated pelites typically carrying their CO_2 and K_2O into the deeper parts of the upper mantle. For the carbonate-bearing protolith considered here, the subsolidus reactions occurring along all P–T paths are the almost isobaric biotite to phengite reaction, which releases H_2O through the partial consumption of zoisite, and the decomposition of amphibole around 80 km depth (at 700°C), producing ~0·5 wt % H_2O. Decarbonation of dolomite occurs at T >750°C near 2·0 GPa, and if dolomite survives to 60 km depth virtually no CO_2 will be released through subsolidus reactions during deeper subduction.

This agrees well with the conclusions based on phase diagram modelling of subducted carbonate-bearing marine sediments (e.g. clay-rich marls) by Kerrick & Connolly (2001) and Connolly (2005). They predicted that carbonate-bearing metasediments are generally volatile conservative and that most of the CO_2 contained in the

sediments will pass the sub-arc depth range. Our experiments demonstrate that melting is necessary to liberate substantial amounts of the K_2O and CO_2; however, the necessary temperatures are exceedingly high for a subduction environment (Kinkaid & Sacks, 1997; Kelemen *et al.*, 2003).

ACKNOWLEDGEMENTS

This work is part of the Ph.D. project of T. B. Thomsen, funded by ETH grant TH 38/02-1. We are grateful to J. A. D. Connolly, P. Ulmer and E. Reusser for discussions that improved the manuscript, and to J. A. D. Connolly and M. Caddick for help with the calculation of the pseudosection. Thanks go to R. Rütti, B. Kuhn and L. Caricchi for assistance with the microprobe, to K. Kunze for help with SEM, and to Signe for her support and patience. Reviews by K. Okamoto and two anonymous reviewers improved significantly a first version of the manuscript, and those by M. Hirschmann, J. Hermann and an anonymous reviewer the final version of the manuscript. Further, we thank J. Hermann for insisting on a comparison of our results with the petrogenetic grid of Hermann (2002), which was not contained in the first versions of the manuscript.

REFERENCES

Auzanneau, E. (2005). Etude expérimentale des relations de phases dans les metasediments à haute pression et haute température. Application à la croute continentale subduite. PhD dissertation, Université Blaise Pascal, Clermont-Ferrand 279 pp.

Auzanneau, E., Vielzeuf, D. & Schmidt, M. W. (2006). Experimental evidence of decompression melting during exhumation of subducted continental crust. *Contributions to Mineralogy and Petrology* **152**(2), 125–148.

Bohlen, S. R., Essene, E. J. & Boettcher, A. L. (1980). Reinvestigations and applications of olivine–quartz–orthopyroxene barometry. *Earth and Planetary Science Letters* **47**, 1–10.

Bose, K. & Ganguly, J. (1995). Quartz–coesite revisited: reversed experimental determinations at 500–1000 degrees C and retrieved thermochemical properties. *American Mineralogist* **80**, 231–238.

Brunsmann, A. F. G. & Heinrich, W. (2002). Experimental investigation of zoisite–clinozoisite phase equilibria in the system CaO–Fe_2O_3–Al_2O_3–SiO_2–H_2O. *Contributions to Mineralogy and Petrology* **143**, 115–130.

Bucher, K. & Frey, M. (2002). *Petrogenesis of Metamorphic Rocks*. Berlin: Springer.

Caron, J.-M. & Pequinot, G. (1986). The transition between blueschists and lawsonite-bearing eclogites based on observations from Corsican metabasalts. *Lithos* **19**, 205–218.

Cawthorn, R. G. & Collerson, K. D. (1974). The recalculation of pyroxene end-member parameters and the estimation of ferrous and ferric iron content from electron microprobe analyses. *American Mineralogist* **59**, 1203–1208.

Comodi, P., Fumagalli, P., Montagnoli, M. & Zanazzi, P. F. (2004). A single crystal study on the pressure behavior of phlogopite and petrological implications. *American Mineralogist* **89**, 647–653.

Connolly, J. A. D. (1990). Multivariable phase diagrams: an algorithm based on generalized thermodynamics. *American Journal of Science* **290**, 666–718.

Connolly, J. A. D. (2005). Computation of phase equilibria by linear programming: A tool for geodynamic modeling and its application to subduction zone decarbonation. *Earth and Planetary Sciences Letters* **236**, 524–541.

Dachs, E. (1986). High-pressure mineral assemblages and their breakdown products in metasediments south of the Grossvenediger, Tauern Window, Austria. *Schweizerische Mineralogische und Petrologische Mitteilungen* **66**, 145–161.

Dachs, E. (1990). Geothermobarometry in metasediments of the southern Grossvenediger area (Tauern Window, Austria). *Journal of Metamorphic Geology* **9**, 61–77.

Dixon, J. E., Clague, D. A., Wallace, P. & Poreda, R. (1997). Volatiles in alkali basalts from the North Arch Volcanic field, Hawaii: extensive degassing of deep submarine-erupted alkalic series lavas. *Journal of Petrology* **38**, 911–939.

Domanik, K. J. & Holloway, J. R. (1996). The stability of phengitic muscovite and associated phases from 5·5 to 11 GPa: implications for deeply subducted sediments. *Geochimica et Cosmochimica Acta* **60**, 4133–4150.

Domanik, K. J. & Holloway, J. R. (2000). Experimental synthesis and phase relations of phengitic muscovite from 6·5 to 11 GPa in a calcareous metapelite from the Dabie Mountains, China. *Lithos* **52**, 51–77.

Domanik, K. J., Hervig, R. L. & Peacock, S. (1993). Beryllium and boron in subduction zone minerals: An ion microprobe study. *Geochimica et Cosmochimica Acta* **57**, 4997–5010.

Droop, G. T. R., Lombardo, B. & Pognante, U. (1990). Formation and distribution of eclogite facies rocks in the Alps. In: Carswell, D. A. (ed.) *Eclogite Facies Rocks*. Glasgow: Blackie, pp. 225–259.

Enami, M., Liou, J. G. & Mattinson, C. G. (2004). Epidote minerals in high P/T metamorphic terranes: subduction zone and high- to ultrahigh-pressure metamorphism. In: Liebscher, A. & Franz, G. (eds) *Epidotes. Mineralogical Society of America, Reviews in Mineralogy and Geochemistry* **56**, 347–398.

Ferry, J. M. (1976). Metamorphism of calcareous sediments in the Waterville–Vassalboro area, south–central Maine: mineral reactions and graphical analysis. *American Journal of Science* **276**, 841–882.

Ferry, J. M. (1983*a*). Regional metamorphism of the Vassalboro Formation, south–central Maine, USA: a case study of the role of fluid in metamorphic pterogenesis. *Journal of the Geological Society, London* **140**(4), 551–576.

Ferry, J. M. (1983*b*). Mineral reactions and element migration during metamorphism of calcareous sediments from the Vassalboro Formation, south–central Maine. *American Mineralogist* **68**, 334–354.

Forneris, J. F. & Holloway, J. R. (2003). Phase equilibria in subducting basaltic crust: implications for H_2O release from the slab. *Earth and Planetary Science Letters* **214**, 187–201.

Frank, E. (1983). Alpine metamorphism of calcareous rocks along a cross-section in the Central Alps: Occurrence and breakdown of muscovite, margarite and paragonite. *Schweizerische Mineralogische und Petrologische Mitteilungen* **63**, 37–93.

Frey, M. (1978). Progressive low grade metamorphism of a black shale formation, central Swiss Alps, with special reference to pyrophyllite and margarite bearing assemblages. *Journal of Petrology* **19**, 93–135.

Green, T. H. & Hellman, P. L. (1982). Fe–Mg-partitioning between coexisting garnet and phengite at high pressure, and comments on the garnet–phengite geothermometer. *Lithos* **15**, 253–266.

Guidotti, C. V. & Sassi, F. (1998). Petrogenetic significance of Na–K white mica mineralogy: Recent advances for metamorphic rocks. *European Journal of Mineralogy* **10**, 815–854.

Guidotti, C. V. & Sassi, F. (2002). Constraints on studies of metamorphic K–Na white micas. In: Mottana, A, Sassi, F. P., Thompson, J. B., Jr & Guggenheim, S. (eds) *Micas: Crystal chemistry and metamorphic petrology, Mineralogical Society of America, Reviews in Mineralogy and Petrology* **46**, 413–448.

Hermann, J. (2002). Experimental constraints on phase relations in subducted continental crust. *Contributions to Mineralogy and Petrology* **143**, 219–235.

Hermann, J. & Green, D. H. (2001). Experimental constraints on high pressure melting in subducted crust. *Earth and Planetary Science Letters* **188**, 149–168.

Holland, T. J. B. & Powell, R. (2002). An internally consistent thermodynamic data set for phase relations of petrological interest. *Journal of Metamorphic Geology* **16**, 309–343.

Holloway, J. R. & Blank, J. G. (1994). Application of experimental results to C–O–H species in natural melts. In: Carroll, M. R. & Holloway, J. R. (eds) *Volatiles in Magmas. Mineralogical Society of America, Reviews in Mineralogy* **30**, 187–230.

Hoschek, G. (1990). Melting and subsolidus reactions in the system K_2O–CaO–MgO–Al_2O_3–SiO_2–H_2O: experiments and petrologic application. *Contributions to Mineralogy and Petrology* **105**, 393–402.

Ishikawa, T. & Nakamura, E. (1994). Origin of the slab component in arc lavas from across-arc variation of B and Pb isotopes. *Nature* **370**, 205–208.

Katayama, I., Parkinson, C. D., Okamoto, K., Nakajima, Y. & Maruyama, S. (2000). Supersilicic clinopyroxene and silica exsolution in UHPM eclogite and pelitic gneiss from the Kokchetav massif, Kazakhstan. *American Mineralogist* **85**, 1368–1374.

Kelemen, P. B., Rilling, J. L., Parmentier, E. M., Mehl, L. & Hacker, B. R. (2003). Thermal structure due to solid-state flow in the mantle wedge beneath arcs. In: Eiler, J. M. (ed.) *Inside the Subduction Factory. Geophysical Monograph, American Geophysical Union* **138**, 293–311.

Kerrick, D. M. & Connolly, J. A. D. (2001). Metamorphic devolatilization of subducted marine sediments and transport of volatiles to the Earth's mantle. *Nature* **411**, 293–296.

Kincaid, C. & Sacks, I. S. (1997). Thermal and dynamical evolution of the upper mantle in subduction zones. *Journal of Geophysical Research* **102**, 12295–12315.

Konzett, J., Frost, D. J., Proyer, A. & Ulmer, P. (2008). The Ca-Eskola component in clinopyroxene as a function of pressure, temperature and bulk composition: an experimental study to 15 GPa with possible implications for the formation of oriented SiO_2-inclusions in omphacite. *Contributions to Mineralogy and Petrology* **155**, 215–228.

Luth, R. W. (1995). Experimental determination of the reaction dolomite + 2 coesite = diopside + 2 CO_2 to 6 GPa. *Contributions to Mineralogy and Petrology* **122**, 152–158.

Massonne, H.-J. & Schreyer, W. (1987). Phengite geobarometry based on the limiting assemblage with K-feldspar, phlogopite and quartz. *Contributions to Mineralogy and Petrology* **96**, 212–224.

Massonne, H.-J. & Schreyer, W. (1989). Stability field of the high-pressure assemblage talc + phengite and two new phengite barometers. *European Journal of Mineralogy* **1**, 391–410.

Massonne, H.-J. & Szpurka, Z. (1997). Thermodynamic properties of white micas on the basis of high-pressure experiments in the systems K_2O–MgO–Al_2O_3–SiO_2–H_2O and K_2O–FeO–Al_2O_3–SiO_2–H_2O. *Lithos* **41**, 229–250.

Molina, J. F. & Poli, S. (2000). Carbonate stability and fluid composition in subducted oceanic crust: an experimental study on H_2O–CO_2 bearing basalts. *Earth and Planetary Science Letters* **176**, 295–310.

Nakamura, D. (2003). Stability of phengite and biotite in eclogites and characteristics of biotite- or orthopyroxene-bearing eclogites. *Contributions to Mineralogy and Petrology* **145**, 550–567.

Ogasawara, Y., Ohta, M., Fukusawa, K., Katayama, I. & Maruyama, S. (2000). Diamond-bearing and diamond-free metacarbonate rocks from Kumdy-Kol in the Kokchetav Massif, northern Kazakhstan. *Island Arc* **9**(3), 400–416.

Ono, S. (1998). Stability limits of hydrous minerals in sediment and mid-ocean ridge basalt compositions: implications for water transport in subduction zones. *Journal of Geophysical Research* **103**(B8), 18253–18267.

Papale, P. (1999). Modeling of the solubility of a two-component $H_2O + CO_2$ fluid in silicate liquids. *American Mineralogist* **84**, 477–492.

Patiño Douce, A. E. (2005). Vapor-absent melting of tonalite at 15–32 kbar. *Journal of Petrology* **46**(2), 275–290.

Patiño Douce, A. E. & Beard, J. S. (1995). Dehydration-melting of biotite gneiss and quartz amphibolite from 3 to 15 kbar. *Journal of Petrology* **36**, 707–738.

Pawley, A. R. (1992). Experimental study of the compositions and stabilities of synthetic nyobite–glaucophane amphiboles. *European Journal of Mneralogy* **4**, 171–192.

Pertermann, M. & Hirschmann, M. M. (2003). Anhydrous partial melting experiments on MORB-like eclogite: phase relations, phase compositions and mineral–melt partitioning of major elements at 2–3 GPa. *Journal of Petrology* **44**(12), 2173–2201.

Plank, T. & Langmuir, C. H. (1998). The chemical composition of the subducting sediment and its consequences for the crust and mantle. *Chemical Geology* **145**, 325–394.

Poli, S. & Schmidt, M. W. (1995). H_2O transport and release in subduction zones: experimental constraints on basaltic and andesitic systems. *Journal of Geophysical Research* **100**, 22299–23314.

Poli, S. & Schmidt, M. W. (1998). The high-pressure stability of zoisite and phase relationships of zoisite-bearing assemblages. *Contributions to Mineralogy and Petrology* **130**, 162–175.

Poli, S. & Schmidt, M. W. (2002). Petrology of subducted slabs. *Annual Review of Earth and Planetary Sciences* **30**, 207–235.

Poli, S. & Schmidt, M. W. (2004). Magmatic epidote. In: Liebscher, A. & Franz, G. (eds) *Epidotes. Mineralogical Society of America, Reviews in Mineralogy and Geochemistry* **56**, 399–430.

Schmädicke, E. & Müller, W. F. (2000). Unusual exsolution phenomena in omphacite and partial melting replacement of phengite by phlogopite + kyanite in an eclogite from the Erzgebirge. *Contributions to Mineralogy and Petrology* **139**, 629–642.

Schmidt, M. W. (1993). Phase relations and compositions in tonalite as a function of pressure: An experimental study at 5650°C. *American Journal of Science* **293**, 1011–1060.

Schmidt, M.W. (1996). Experimental constraints on recycling of potassium from subducted oceanic crust. *Science* **272**, 1927–1930.

Schmidt, M. W. & Poli, S. (1998). Experimentally based water budgets for dehydrating slabs and consequences for arc magma generation. *Earth and Planetary Science Letters* **163**, 361–379.

Schmidt, M. W., Vielzeuf, D. & Auzanneau, E. (2004). Melting and dissolution of subducting crust at high pressures: the key role of white mica. *Earth and Planetary Science Letters* **228**, 65–84.

Schultze, D. J., Valley, J. W. & Spicuzza, M. J. (2000). Coesite eclogites from the Roberts Victor kimberlite, South Africa. *Lithos* **54**, 23–32.

Shatsky, V., Sobolev, N. V. & Vavilov, M. A. (1995). Diamond-bearing metamorphic rocks of the Kokchetav Massif (northern Kazakhstan). In: Coleman, R. G. & Wang, X. (eds) *Ultrahigh*

Pressure Metamorphism. Cambridge: Cambridge University Press, pp. 427–455.

Sorensen, S. S. (1986). Petrologic and geochemical comparison of the blueschist and greenschist units of the Catalina Schist terrane, southern California. In: Evans, B. W. & Brown, E. H. (eds) *Blueschists and Eclogites. Geological Society of America, Memoirs* **164**, 59–75.

Spear, F. S. (1995). *Metamorphic Phase Equilibria and Pressure–Temperature–Time Paths. Mineralogical Society of America, Monograph* **1**.

Thompson, A. B. (1975). Mineral reactions in a calc-mica schist from Gassetts, Vermont, U.S.A. *Contributions to Mineralogy and Petrology* **53**, 105–127.

Thompson, A. B. (1988). Dehydration melting of crustal rocks. *Rendiconti della Società Italiana di Mineralogia e Petrografia* **43**, 41–60.

Thomsen, T. B. (2006). Micas in carbonate-saturated pelites: The transformation from biotite to phengite, melting and melt geochemistry. Ph.D. dissertation, ETH-Zürich, 124 pp.

Thomsen, T. B. & Schmidt, M. W. (2008). Melting of carbonated pelites at 2·5–5·0 GPa, silicate–carbonatite liquid immiscibility, and potassium–carbon metasomatism of the mantle. *Earth and Planetary Science Letters* **267**, 17–31.

Velde, B. (1965). Phengite micas: synthesis, stability, and natural occurrence. *American Journal of Science* **263**, 886–913.

Velde, B. (1966). Si^{+4} content of natural phengites. *Contributions to Mineralogy and Petrology* **14**, 250–258.

Velde, B. (1967). Upper stability of muscovite. *American Mineralogist* **51**, 924–929.

Vielzeuf, D. & Holloway, J. R. (1988). Experimental determination of the fluid-absent melting relations in the pelitic system. Consequences for crustal differentiation. *Contributions to Mineralogy and Petrology* **98**, 257–276.

Vielzeuf, D. & Schmidt, M. W. (2001). Melting relations in hydrous systems revisited: Applications to pelites, greywackes and basalts. *Contributions to Mineralogy and Petrology* **141**, 251–267.

Wallace, P. & Anderson, A. T. (1999). Volatiles in magmas. In: Sigurdsson, H., Houghton, B., Rymer, H., Stix, J. & McNutt, S. (eds) *Encyclopedia of Volcanoes*. New York: Academic Press, pp. 149–170.

Winther, K. T. & Newton, R. C. (1991). Experimental melting of hydrous low-K tholeiite: evidence on the origin of Archean cratons. *Bulletin of the Geological Society of Denmark* **39**, 213–228.

Wunder, B. & Melzer, S. (2002). Interlayer vacancy characterization of synthetic phlogopitic micas by IR-spectroscopy. *European Journal of Mineralogy* **14**(6), 1129–1138.

Zhang, R. Y., Liou, J. G. & Cong, B. L. (1995). Talc-, magnesite- and Ti-clinohumite-bearing ultrahigh-pressure meta-mafic and ultramafic complex in the Dabie Mountains, China. *Journal of Petrology* **36**, 1011–1037.

Zhang, R. Y., Liou, J. G., Ernst, W. G., Coleman, R. G., Sobolev, N. V. & Shatsky, V. S. (1997). Metamorphic evolution of diamond-bearing and associated rocks from the Kokchetav Massif, Northern Kazakhstan. *Journal of Metamorphic Geology* **15**, 479–496.